

Understanding interfacial energy structures in organic solar cells using photoelectron spectroscopy: A review



Cite as: J. Appl. Phys. 132, 050701 (2022); doi: 10.1063/5.0091960

Submitted: 18 March 2022 · Accepted: 28 June 2022 ·

Published Online: 5 August 2022



View Online



Export Citation



CrossMark

Ju Hwan Kang,¹ Jin Hee Lee,² Bright Walker,³ Jung Hwa Seo,^{1,a)} and Gap Soo Chang^{4,a)}

AFFILIATIONS

¹ Department of Physics, University of Seoul, Seoul 02504, Republic of Korea

² Department of Chemical Engineering (BK21 FOUR), Dong-A University, Busan 49315, Republic of Korea

³ Department of Chemistry, Kyung Hee University, Seoul 02447, Republic of Korea

⁴ Department of Physics and Engineering Physics, University of Saskatchewan, Saskatoon, SK S7N 5E2, Canada

^{a)} Authors to whom correspondence should be addressed: seojh@uos.ac.kr and gapsoo.chang@usask.ca

ABSTRACT

Organic solar cells (OSCs) have received considerable attention as a promising clean energy-generating technology because of their low cost and great potential for large-scale commercial manufacturing. With significant advances in new charge-transport material design, interfacial engineering, and their operating conditions, power conversion efficiencies of OSCs have continued to increase. However, a fundamental understanding of charge carrier transport and especially how ionic moieties affect carrier transport is still lacking in OSCs. In this regard, photoelectron spectroscopy has provided valuable information about interfacial electronic structures. The interfacial electronic structure of OSC interlayers greatly impacts charge extraction and recombination, controls energy level alignment, guides active layer morphology, improves material's compatibility, and plays a critical role in the resulting power conversion efficiency of OSCs. Interfacial engineering incorporating inorganic, organic, and hybrid materials can effectively enhance the performance of organic photovoltaic devices by reducing energy barriers for charge transport and injection while improving compatibility between metal oxides and donor–acceptor based active layers or transparent conducting electrodes. This article provides a review of recent developments in interfacial engineering underlying organic photovoltaic devices of donor–acceptor interfaces.

Published under an exclusive license by AIP Publishing. <https://doi.org/10.1063/5.0091960>

I. INTRODUCTION

Organic solar cells (OSCs) represent one of several advancing technologies for renewable energy conversion, converting solar energy directly into electricity. OSCs based on a broad family of molecular semiconducting structures including small molecules such as fullerenes and non-fullerenes as well as polymers have attracted tremendous interest over the past three decades. Much effort has been devoted to material design,^{1–6} device engineering,^{7–12} morphology optimization,^{13–18} and mechanistic studies^{19–21} and have led to steadily increasing power conversion efficiencies (PCEs). Among different research areas, controlling the interfaces between the photoactive layer and the electrodes in OSCs contributes significantly to achieving high PCEs. A large proportion of research has focused on developing new interlayer materials with stable physical properties

and adequate energy levels aligned at the interfaces to increase charge selectivity at the corresponding electrodes and prevent undesirable charge recombination.

Interfaces must be correctly engineered in order to create desirable electrical contacts between photoactive layers; the properties of these interfaces in OSCs largely determine the dynamics of charge carrier recombination.^{22–24} Interfacial layers can be used to control the energy band structures and achieve ohmic contacts at organic/metal, organic/semiconductor, and electrode/organic interfaces.^{25,26} Interfacial materials also serve as surface protective layers among other roles. The thin films (<1 μm) used in OSCs must be considered in terms of their bulk and volume-occupying material properties as well as their surface properties; however, the surface characteristics dominate as the film thickness decreases.

Built-in potentials are generated at the cathode and anode electrode interfaces and create a driving force that causes positive and negative charge carriers to drift in opposite directions and be selectively collected at each electrode.^{27–32} Inappropriately designed intermediate layers can lead to severe charge carrier recombination, while proper use of intermediate layers can reduce energy barriers and block back-diffusion of opposite charge carriers, thereby inhibiting recombination by efficiently collecting charge carriers. Thus, in order to extract carriers, interfacial materials are critical to minimize the energy barriers between photo-active layers and electrodes.

Interfacial materials are broadly classified into three categories: ionic and electrolytic materials, metal oxides, and hybrid materials. Currently, some of the most commonly used ionic and electrolytic materials include conjugated polyelectrolytes (CPEs)³³ and non-conjugated polyelectrolytes (NPEs)^{34–36} such as [(9,9-bis(3'-(N,N-dimethylamino)propyl)-2,7-fluorene)-alt-2,7-(9,9-diocetylfluorene)] (PFN)^{37,38} and polyethyleneimine (PEI),³⁹ which may be used to control the properties of junctions formed between electrodes and photoactive layers. Polyelectrolytes, including both CPEs and NPEs, have several unique advantages. Their good solubility in polar solvents, including water and alcohol, makes them environmentally friendly and allows them to be easily deposited onto electrodes or substrates by low-temperature solution processes. Additionally, the solubility of CPEs and NPEs in relatively polar solvents has opened up the possibility to the solution-process for multilayer structures. Since most of the *n*-type polyelectrolytes developed so far are only effective in lowering the work function (WF) of the electrodes, most reported ionic polymers have been utilized as electron transport layers (ETLs) for enhancing electron carrier collection at the cathode, whereas ionic polymers have been scarcely studied as a hole-transport layers (HTLs).

The WF is a critical concept in the context of not only OPVs, but all types of semiconducting materials and devices. The WF is defined as the minimum amount of work or energy that is required to remove an electron from a solid material to a point immediately outside the solid's surface, where the electron can be considered as a free, unbound electron. The WF depends largely on the energy of the highest occupied electronic orbital in the material and is influenced by local charges and electric fields near the electron, which can affect the amount of energy required to remove it from the solid due to electrostatic interactions. As gases and molecules adsorbed to a material's surface can affect the local electrical potential at the surface, the WF is defined for the surface of a material in a vacuum and measurements of the WF must be carried out under high vacuum. The WF of a material can be thought of as a kind of quantitative measure of how energetically stable valence electrons in a material are and can be used to predict which way electrons will move when a junction is formed between two materials with different WFs. When two electrodes with different WFs come in contact with a semiconductor, some electrons from the electrode with the lower WF will transfer to the electrode with the higher WF until charges accumulate on the two electrodes with a difference in the electrical potential equivalent to the difference in the WF of the two electrodes. This effect is exploited in solar cells, where the electric field created between two electrodes with different WFs drives electrons and holes to drift in opposite directions after being photo-generated.

Recently, it has been demonstrated that the WF of indium tin oxide (ITO) can be increased by depositing copper (Cu)-based polyelectrolytes as HTLs and that OSCs fabricated from the poly-electrolyte Cu(II) poly(styrene sulfonate) (Cu:PSS) showed an improved PCEs.⁴⁰ When this polyelectrolyte is deposited as a thin layer (>10 nm), it is able to increase the WF of substrates and improve the hole extraction by causing desirable band-bending at the anode interface.

A number of metal oxides, particularly those wide-bandgap metal oxides such as titanium dioxide (TiO_2),⁴¹ zinc oxide (ZnO),^{42,43} molybdenum oxides (MoO_x),^{44,45} and nickel oxide (NiO)^{46,47} have found wide applications in sustainable clean energy, including solar cells and energy storage devices, due to their natural abundance, easy synthesis, high stability, unique optical/electronic properties, and excellent photoelectric and electrochemical properties.^{48,49} In order to achieve low contact resistance between the electrode and the photoactive layer, transition metal oxides having high transparency in the visible and near infrared spectral regions have been studied in OSCs. Metal oxides have been used as both ETL and HTL materials for the OSCs; the distinction between these two types is contingent on the relative positions of the lowest unoccupied molecular orbital (LUMO) of the acceptor in the light-absorbing layer, and the highest occupied molecular orbital (HOMO) of the donor in the light-absorbing layer. For ETL materials, electron transfer from the LUMO of the acceptor to the conduction band of the metal oxide is requisite, while for HTL materials such as vanadium oxide (V_2O_5) and NiO , the valence band of the metal oxide should be aligned with the HOMO of the polymer.

Organic-inorganic hybrid materials comprise combinations of organic and inorganic components, such as mixtures of conjugated polymers and inorganic semiconductors, like TiO_2 , ZnO , carbon nanotubes, and graphene. These hybrid materials have attracted scientific as well as practical attention owing to their combination of advantages including high electron affinity³⁰ and stability^{50,51} of inorganic semiconductors with the flexibility of polymers. TiO_2 has been extensively studied as an electron acceptor for fabricating OSCs, because it is a chemically safe, environmentally stable, and low-cost material. Graphene, an exclusive two-dimensional nanostructure with unique mechanical, optical, and electronic properties, is considered one of the most attractive materials for use in various types of solar cells.^{52–54} Functionalization is a very important strategy for developing novel hybrid materials with new and transformed properties. Characteristics of various carbon-based nanomaterials such as fullerene,⁵⁵ carbon nanostructures,⁵⁶ carbon nanotubes,⁵⁷ and graphene may be improved by adding a molecular part having desired characteristics for a specific application field. According to a study by Kang *et al.*, a proper alignment of energy levels in different components can be achieved by incorporating Cu metal on graphene to control charge generation, movement, and recombination, which are very important parameters in semiconducting devices including OSCs. The types of dopant materials and carbon-based nanomaterials, and the chemical properties of linkers can all contribute to the final performance of the device.⁵⁸

This review article provides an overview of performance-enhancement strategies for OSCs with a focus on energy band structure; it is organized into sections that introduce principles of

interfacial engineering and energy band structures, then covers specific examples from categories of organic, inorganic, and hybrid materials, from the perspective of electronic structure engineering. The first section introduces the reader to the concept of OSCs, detailing the device structure and energy level alignment in OSCs. Sections II and III introduce the electronic structures of organic materials and a detailed introduction to photoelectronic spectroscopy, respectively. In Sec. IV, characteristics of interfacial materials are explored and a comprehensive list of electronic structures based on interfacial materials that have been successfully implemented is presented. Finally, we provide summaries and perspectives for electronic structure engineering of interfacial materials in Sec. V.

II. INTERFACIAL ENGINEERING FOR OSCS WITH INVERTED AND CONVENTIONAL STRUCTURE

The solution processability of organic materials is one of the most attractive advantages of OSCs, which makes OSCs suitable for large-area production via scalable printing technologies at a low cost.^{59–63} As shown in Figs. 1(a) and 1(b), a typical single-junction OSC device usually consists of two electrodes, interfacial layers, and a light-harvesting layer. In addition to the functions of charge collection and transport, one of the electrodes should be transparent to ensure efficient transmission of photons to the active layer. The other electrode is usually aluminum or silver, which can reflect unabsorbed light through the active layer again. Both electrodes are usually modified with interface layers, namely, anode and cathode interfacial layers, to optimize the electronic band structure at the interfaces between the light-harvesting active layer and the charge-collecting electrodes. OSCs have higher exciton binding energies (typically ~ 0.5 eV)^{64,65} so that it is difficult to separate excitons into mobile charge carriers at room temperature. Therefore, OSCs generally consist of a blended structure comprising an electron donor and an electron acceptor, where excitons created by photon

absorption are separated into mobile charge carriers at the interface between these two phases. Since diffusion distance of excitons is only about 10 nm, the geometric form of the blend structure is very important to ensure most excitons to produce separated charges, and that the separated electrons can be extracted via continuous pathways through each phase.

When light is irradiated on the surface of an organic semiconductor, photons interact with the electrons in the molecular orbitals corresponding to the conjugated π -bonding system in the absorbing material. When a negatively charged electron is excited to a higher energy orbital by absorbing energy from a photon, it leaves a hole, or a positive charge carrier, in the original orbital. At this point, organic semiconductor exists in an associated electron-hole state called an exciton, caused by photoexcitation. In organic materials, excitons cannot be easily dissociated into mobile positive and negative charge carriers with thermal energy alone; at least two different organic semiconductors are needed to provide a thermodynamic driving force to separate the excitons by overcoming their binding energy (E_b). If the energy state of charge carriers in two separate semiconductor phases is more stable than the excitonic state by a difference which is greater than E_b , the exciton may dissociate at the interface between them. Organic active materials are classified into donors and acceptors depending on whether a material donates electrons and carries positive mobile charges (holes) or accepts electrons and carries negative mobile charges (electrons), respectively. The working principle of OSCs can be summarized as four steps required for the generation of electric power via the absorption of incident light. (1) Photoinduced exciton generation, (2) exciton diffusion to the interface, (3) exciton dissociation and hole transfer into the HOMO of the donor and electron transfer into the LUMO of the acceptor, and (4) collection of electrons and holes at the external electrodes.

There are various strategies to improve device characteristics so that the greatest amount of electricity can be extracted from OSCs, but one of the most effective strategies is to introduce interfacial layers.⁶⁶ In an OSC, interfacial engineering is critical to forming adequate contacts between photoactive layers by placing appropriate layers at the interfaces of the donor:acceptor mixture and the electrodes.^{67,68} The interfacial layers can allow the formation of ohmic contacts that minimize energetic barriers to charge carrier extraction, while blocking opposite charge carriers and excitons from recombining at the electrodes. In addition, the interfacial materials serve as a protective layer that ensures the stability of OSCs by preventing penetration or pinholes at the interfaces and buffering unwanted chemical degradation that may occur over time, when the photoactive layer is in direct contact with metals or ITO electrodes. In general, interfacial materials can be largely classified as HTLs or ETLs, according to their structure and position in the device. Figures 1(c) and 1(d) represent band diagrams for two device architectures. One of the main loss mechanisms in these devices is the reverse diffusion of charge carriers. In OSCs, electrons should drift to the cathode, while holes drift to the anode; however, backwards diffusion of these carriers can result in recombination with oppositely charged carriers within the active layer or at the interfaces, resulting in energy loss. Two principal regimes for charge carrier recombination can be identified in OSCs. They include geminate recombination and bimolecular recombination.

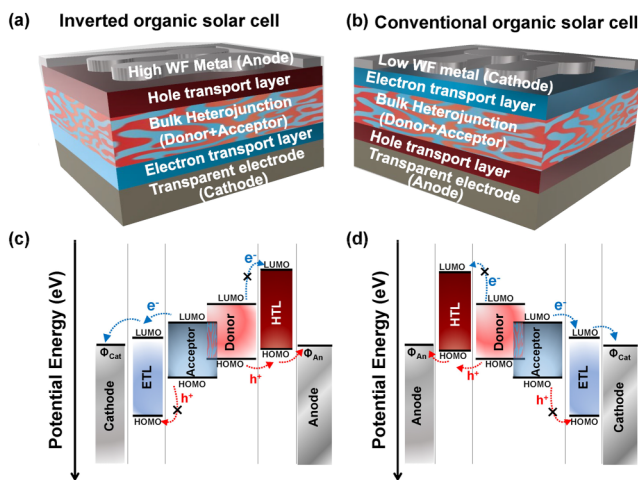


FIG. 1. Device architectures of (a) an inverted and (b) conventional OSCs. The energy level alignments of (c) the inverted and (d) the conventional OSCs with ohmic contacts at the both electrodes.

Geminate recombination involves the recombination of an electron and a hole created by the same photon and is related to non-optimal charge separation following charge transfer at the donor/acceptor interface. Geminate recombination is often a major issue in polymer-polymer structures, but it is not as problematic in polymer/fullerene structures which tend to exhibit good long-range charge separation after photoinduced electron transfer. In most contemporary OSC devices, geminate recombination can be minimized by choosing appropriate donor:acceptor combinations, thereby making bimolecular recombination the dominant mechanism for charge recombination. Bimolecular recombination occurs when free positive and negative charge carriers recombine nonradiatively; it is an encounter-limited reaction where the average time for an electron and a hole to meet in the film determines the recombination rate. A larger population of electrons and holes increases the probability that they will encounter each other so that the bimolecular recombination rate depends on the concentration of charge carriers. Additionally, the recombination coefficient is strongly dictated by the mobility of the charge carriers, where higher mobilities decrease the amount of time for charge carriers to exit the active layer. Currently, bimolecular recombination tends to be the dominant loss process that limits the PCE in the best bulk heterojunction (BHJ) OSCs. Therefore, ETL and HTL constitute an essential class of interfacial materials in OSC and are one of the most commonly investigated types of interfacial materials.

III. PHOTOELECTRONIC SPECTROSCOPY

A detailed understanding of the electronic structure at the device interfaces is the key to a deliberate and insight-driven optimization.^{69,70} Photoelectron spectroscopy (PES) provides a unique perspective into the electronic structure at the interfaces. Although this review is focused on OSCs, which are comprised mainly of organic semiconductors, PES is a versatile tool that can be used to understand the electronic structure of any kind of solid materials, including metals, semiconductors, and insulators. It can be used with organic, inorganic, and hybrid materials and provides information that is relevant to a multitude of applications beyond solar cells, including diodes, transistors, batteries, and even in non-electronic contexts such as structural materials. Thus, being able to understand PES data can improve one's understanding of a diverse range scientific discipline and is like a passport allowing access to innumerable opportunities for interdisciplinary collaboration. PES spectra, which quantify E_b of electronic bands in a solid sample, directly reflect the electronic (i.e., molecular orbital) structure of organic molecules or polymers as described by Koopmans' theorem that the electronic structure of the ionized state is well-approximated by the electronic structure of the initial (non-ionized) molecule.^{71,72} It should be noted that the ionization energy is not exactly the same as the HOMO level. Ionization potential (IP) can be measured experimentally, while a HOMO energy is a theoretical concept that has sense only within the one-electron approximation (such as in the Hartree-Fock theory). In practice, actual solid materials measured using PES consist of many individual molecules packed together in the solid state with many electrons. The IP of the sample provides a quantitative measure of the energy difference between highest occupied

electronic state in the sample and the vacuum level, which is strongly dependent on the HOMO levels of the molecules which make up the sample. Again, this IP measurement is not identical to the HOMO level but provides a quantitative, measurable approximation as stated in the Koopmans' theorem. Likewise, the electron affinity of a material, which is an experimentally measurable quantity, can be correlated to the energy of the conceptual LUMO level. The ability to extract both initial and final state information from PES data is particularly interesting for systems, where reduction and oxidation processes are chemically meaningful. For reduction and oxidation active species, PES is a direct probe of oxidation processes and can thus evaluate the effect of electronic structure on reduction and oxidation processes directly. It further allows experimentalists to evaluate changes in the electronic structure occurring as a result of reduction and oxidation events, i.e., PES is a direct probe of electronic relaxation upon ionization.

In x-ray photoelectron spectroscopy (XPS), x-ray photons are used to probe the elemental distribution within a solid thin film. The physical basis of the XPS technique is illustrated in Fig. 2(a). When a solid surface is irradiated with soft (energy less than ~ 5 keV) x-ray photons, incident photons of energy $h\nu_1$ can be absorbed by an electron with E_b below the vacuum level (E_{VAC}). The entire photon energy is transferred to the electron, which is promoted to a higher energy state. If E_b of the electron is less than $h\nu_1$, it will be promoted to an energy state above E_{VAC} . As a result, this photoelectron is ejected into vacuum with kinetic energy ($E_k = h\nu_1 - E_b$). PES using an x-ray source allows the observation of core-level electrons with relatively high binding energies compared to valence electrons, which can be photoionized by high energy of the x rays. E_b of the core electrons and resultant E_k of the ejected

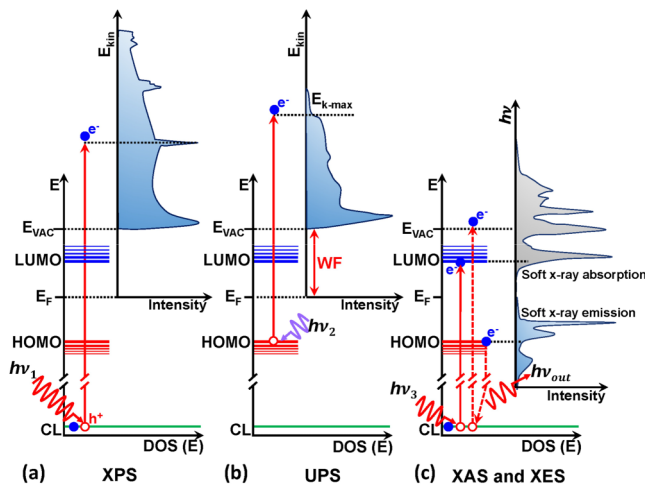


FIG. 2. Schematic presentations of the ground-state electronic structure (left side) and simplified spectrum (right side) in (a) XPS, (b) UPS, and (c) XAS and XES. (E_{VAC} : the vacuum level, E_F : the Fermi level, HOMO: the highest occupied molecular orbital, LUMO: the lowest unoccupied molecular orbital, CL: the core level, DOS: the energy-dependent density of states, and WF: work function.) Blue and gray shadings indicate occupied and unoccupied electronic states, respectively.

photoelectrons depend on the chemical state (i.e., oxidation state and bond order of each atom) of the sample. Therefore, XPS of core levels can often be used for chemical analysis and the name electron spectroscopy for chemical analysis (ESCA) has been given for this technique.

If an element exhibits multiplet splitting during photoelectron emission due to different spin states, this can cause the apparent energy to change due to spin-orbit splitting. This can lead to misinterpretation of XPS data when spin-orbit splitting effects are disregarded, when the proper intensity ratio for a pair of spin-orbit split peaks are neglected, and/or when only spin-orbit splitting for a fraction of the fit components are considering for a peak envelope. In many cases, spin-orbit peaks are incorrectly labeled as separate chemical states. Area and position constraints for doublet peaks are well defined and should be used when constructing peak models that include doublet pairs. The use of reference databases for understanding expected spin-orbit properties such as energy splitting, intensity ratios, and FWHM differences can help to minimize erroneous interpretation of spin-orbit effects. Additionally, such databases can provide appropriate constraints that should be considered to define the properties of synthetic peaks for the construction of the fitting curves.

Ultraviolet photoelectron spectroscopy (UPS) is a very surface-sensitive technique due to the short inelastic mean-free path of the photoelectrons (defined as the $1/e$ attenuation length), in the order of 1–3 nm for excitation in the ultraviolet (UV) range. However, the mean-free path is still sufficient for electrons originating inside the bulk of the solid to reach the surface and be detected. In UPS, a sample is excited by UV photons with energy $h\nu_2$ (typically from a helium discharge lamp with $h\nu_2 = 21.2$ eV, but other wavelengths are possible), emitting an electron (the “photoelectron, e^- ”) from an occupied electronic state [Fig. 2(b)]. The ionization potential (IP) or HOMO level of an organic semiconductor can be determined through UPS measurement, which yields the energy levels of occupied electronic bands due to valence electrons. When an electron is excited from its ground state to the vacuum level, a photoelectron is emitted, and the kinetic energy of the photoelectron is measured. The electron’s kinetic energy is correlated with the energy of the molecular orbital energy, and the photon energy is equal to the sum of the electron’s absolute kinetic energy and its orbital potential energy. An electron from the HOMO has the highest kinetic energy ($E_k = h\nu_2 - E_{\text{HOMO}}$), where $h\nu_2$ is the UV photon’s energy and E_k is the highest kinetic energy. The WF is the energy necessary to remove one electron from the surface of a material based on the photoelectric effect. To determine the WF of a particular material, which is a typical operation in an interface survey, the entire spectrum must be measured up to the secondary electron cut-off as shown in Fig. 2(b). The spectrum starts at the Fermi edge at 0 eV for metal samples and ends at the point where electrons with nearly zero kinetic energy leave the sample. The WF of the material can now be determined by subtracting the width of the spectrum from the photon energy. The intensity of the incident light and $E_{k,\text{max}}$ ⁷⁰ may be used to calculate WF using the equation $\text{WF} = h\nu_2 - E_{k,\text{max}}$. The IP of an organic semiconductor is determined by the energy difference between the incident UV photon and the generated photoelectron. In this way, UPS can be used to analyze the hole injection barrier (ϕ_h) between the substrate and the HOMO level of an

organic semiconductor deposited on top of the substrate by measuring the IP of the substrate and the organic semiconductor.

In practice, when photoelectrons are ejected from organic semiconductors for the collection of PES spectra, positive charge may be built up on the sample due to relatively low charge carrier mobilities, low conductivities, and semi-insulating nature of these materials. In this case, all detectable photoelectron peaks from all levels and all elements present within a sample may shift by the same amount to higher binding energies. In extreme cases, these peaks become part of the background signal. This problem can be resolved by charge compensation or replacement of emitted electrons by negatively charging the sample. These processes effectively cause shifts in the x axis of photoelectron spectra, which can be corrected by comparison to an internal standard in the sample with a well-known E_b .

Another useful type of information that can be derived from XPS is the film thickness. If a film is less thicker than the sampling depth of photoelectrons and spectral difference can be discerned between the film and underlying substrate, the film thickness can be determined. Indeed, very precise measurements can be carried out on uniform films through a modification of the Beer-Lambert law. The thickness, d of each deposited layer is given by

$$d = -l \left[\ln \left(\frac{I}{I_0} \right) \right], \quad (1)$$

where l is the mean free path of the emitted electrons, I is the intensity measured on each film, and I_0 is the intensity measured on the bare substrate (typically Au).

Figure 2(c) shows the principles of soft x-ray absorption and emission spectroscopy (XAS and XES, respectively). In XAS, the sample is illuminated with x rays and their energy is scanned across a range of energies corresponding to a specific core energy level. An electron from the core level is then excited into an unoccupied electronic state. For semiconductors, the spectra contain valuable information about the conduction band, unoccupied electronic states, and the chemical environment of the probed atoms, which can be selected by choosing the corresponding absorption edges. Depending on the setup and purpose of the experiments (e.g., the desire for high or low surface sensitivity), specific “yield” modes are chosen, for which most commonly electrons or x rays emitted from the sample are detected as a function of exciting photon energy. The occupied states of XES can be used to analyze the chemical and electronic structure of materials.^{72–74} For XES, a core-level electron is excited by x-ray photons, which populates outer empty electronic states. Outer-state electrons then relax to fill the produced core hole states, causing photons to be emitted and detected by an x-ray spectrometer. The cross section for this process (compared to that for direct photoemission) is extremely narrow, necessitating the use of high-flux synchrotron light sources for the studies. XES is a good instrument for probing the local structure of a given atomic center since the radiative relaxation process depends strongly on the chemical environment around the produced core hole.

IV. INTERFACIAL ELECTRONIC STRUCTURES IN OSCs

Recent progress with BHJ OSCs containing mixtures of conjugated copolymers and non-fullerene acceptors has led to OSCs

with impressive performance.^{75–82} In particular, optimization of the self-assembly and morphology of mixed films,^{65,83} new charge transport material design,⁸⁴ interfacial control,⁸⁵ and efficient device architectures have been attempted for the improvements in PCEs. In order to extract electric charges more efficiently, interfacial engineering strategies that minimize the interfacial energy barriers for charge carriers traversing each layer must be selected. Complex phases appear at the interface between organic materials and metals, and various interfacial materials are used due to their electric energy alignment at the interface. These energy band structures are complicated by materials containing strong dipoles or ions, which result in interfacial dipoles.^{86–92} Interfacial dipoles can make the vacuum energy shift and cause band-bending effects. However, these effects can advantageously improve carrier extraction as well. We will discuss three types of interfacial materials in terms of their structures, including organic, inorganic, and hybrid materials.

A. Ionic and electrolytic materials (organic materials)

CPEs are a class of macromolecules that contain a π -conjugated backbone, an ionically functionalized alkyl side chain and a counterion.⁹³ These polymer-based interlayers form extremely thin interfacial dipoles, which can alter the electrode's WF and facilitate the charge transport to electrodes.^{94,95} The delocalized π -electrons in the CPE backbone confer the optical and charge transport properties of organic semiconductors.^{96–98} In addition, the charged group of the side chain gives CPEs relatively high dielectric constants and imbues solubility in polar solvents and water. CPEs are classified as cationic and anionic CPE according to the type of ions attached to the backbone.^{99,100}

Liu *et al.* in 2017 developed a series of fluorinated CPEs as ETLs for inverted solar cells and found that engineering of the junction backbone had a significant impact on the interfacial dipole of the electrode/active layer, the conductivity, and the morphology of the CPE.¹⁰¹ Novel alcohol-soluble CPEs were synthesized by incorporating fluorinated benzene moieties into the backbone, namely, poly(9,9'-bis(6"-N,N,N-trimethylammoniumhexyl)fluorene-alt-fluorobenzene) (PFf_1B) and poly(9,9'-bis(6"-N,N,N-trimethylammoniumhexyl)fluorene-alt-tetrafluorobenzene) (PFf_4B), to control the interfacial dipole. PFf_1B and PFf_4B based on fluorene and fluorobenzene were synthesized by introducing different numbers of fluorine atoms into the conjugated skeleton. The incorporation of fluorine atoms into the backbone of active layers is a promising and widely used technique for molecular design. Fluorine has a relatively small van der Waals radius and is the most electronegative element with a Pauling electronegativity of 4.0 (the highest among the halogen group), which provides a strong inductive electron-withdrawing effect. This effect can increase E_b of the HOMO and LUMO levels while also causing non-covalent attractive interactions between nearby moieties, molecule self-assembly, and dipole-dipole interactions. As the number of substitutions of F atoms increased in the ITO/ETLs/poly(3-hexylthiophene-2,5-diyl) (P3HT):[6,6]-phenyl-C₆₁-butyric acid methyl ester (PC₆₁BM)/MoO₃/Ag devices, PCEs progressively improved from 2.44% for PFB to 2.73% for PFf_1B and 3.24% for PFf_4B . The key to improved device efficiency appears to be the dipole effects caused by the electronic structure and

WF change of the CPE-modified ITO electrode. XPS and UPS results quantified the changes in the WF and interfacial dipoles of CPE modified ITO electrodes. As shown in Fig. 3(a), the WFs of ITO substrates were modified to 4.12 eV (by -0.58 eV) for PFB, to 3.97 eV (by -0.73 eV) for PFf_1B , and to 3.89 eV (by -0.81) for PFf_4B , compared to that of bare ITO (4.70 eV). The significant difference in WF between the three CPEs demonstrates the strong influence of fluorination of the conjugated backbone on the interfacial dipole. Fluorinated CPEs have been found to have dipoles derived from N^+/O^{2-} ion interactions and F-H-O bonding on ITO, creating dipoles at the ITO/CPE interface away from ITO and substantially reducing the effective WF of ITO [Fig. 3(b)]. The electronegative F atoms create polar bonds and have a strong influence on the dipole formation [as depicted in Fig. 3(c)] as well as being a crucial factor in the electrostatic self-assembly on the ITO surfaces. It is there expected that those aspects presumably yield a larger WF reduction for the ITO/ PFf_nB cathode than the ITO/PFB cathode. High electron affinity of the F atom caused negative charge carriers in the conjugated backbone to be stabilized, while pendant positive charges electrostatically compensated these charges, leading to *n*-type self-doping. Self-doping was confirmed in these CPEs, leading to a large interfacial dipole and desirable effects on the band structure.

CPEs generally require expensive starting materials, combined with delicate and complex synthetic procedures. On the other hand, NPEs can be synthesized simply and inexpensively while functioning as ionic interfacial materials without interfering effects that may arise from π -conjugated backbones.^{39,102,103} The effects of NPEs on electronic band structures occur purely due to ionic interactions without introducing an additional semiconducting material (i.e., the conjugated backbone in CPEs), which may convolute the effects of the ionic functionalities. For example, Kang *et al.* reported three non-CPEs based on protonated PEI with different types of counterions [Fig. 4(a)] such as bromide (Br^-), iodine (I^-), and tetrakis(imidazolyl) borate (BIm_4^-), and systematically investigated the size effect of counterions on their performance as *n*-type NPEs acting as cathode ETLs in inverted OSCs.³⁶

The device performance was correlated well with the magnitude of the interfacial dipole created by each polyelectrolyte ($\text{Br}^- < \text{I}^- < \text{BIm}_4^-$). Improved ohmic contacts caused by the interlayers and the diminished energy loss between the ITO and the active layer were controlled by the incorporation of the *n*-type NPEs with variable-sized counterions as interlayers, and the PCE was improved up to 6.77% with $\text{PEIH}^+\text{BIm}_4^-$, compared to 1.05% without an ETL. In addition, the OSC performance was also affected by film morphology, where the roughest films (PEIH^+I^-) yielded slightly lower performance than smoother PEIH^+Br^- films. Figure 4(b) shows the XPS N 1s core level spectra of PEIH^+Br^- and PEIH^+I^- films, featuring a peak at 403.3 eV, consistent with quarternized N^+ . Additionally, Br and I 3d spectra confirmed the anionic chemical states of Br^- and I^- counterions. UPS confirmed the decreased WF of ITO (4.47 eV after applying the $\text{PEIH}^+\text{BIm}_4^-$ ETL) indicating that the ETL improved electron extraction compared to the bare substrate due to the formation of an interfacial dipole [Fig. 4(c)]. Figure 4(d) presents a schematic diagram of the interfacial dipole generated by $\text{PEIH}^+\text{BIm}_4^-$ lowering the WF of the cathode by 0.23 eV.

While most reported CPE and NPEs have been used as ETL layers due to the majority of these materials containing amines and

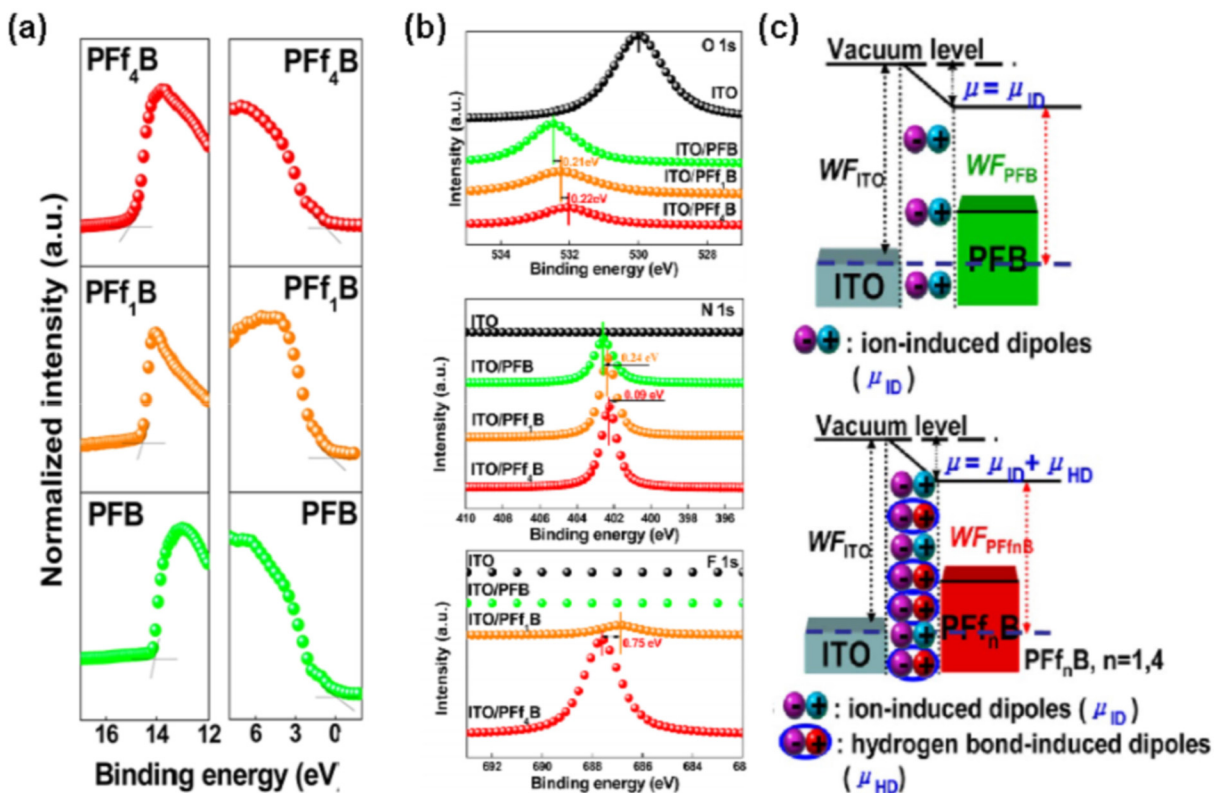


FIG. 3. (a) UPS spectra of PFB, PFf₁B, and PFf₄B on ITO. (b) XPS spectra of O 1s, N 1s, and F 1s on the surface of PFB, PFf₁B, and PFf₄B on the ITO substrate. (c) Schematic illustrations and corresponding energy level diagrams of the interfaces between the ITO and PFf₄B, PFf₁B, and PFB. Reproduced with permission from Liu et al., ACS Appl. Mater. Interfaces 9, 1145 (2017). Copyright 2017 American Chemical Society.

ammonium cations, which predominantly form the interfacial dipoles decreasing the WF and favoring the electron extraction, HTL research has less frequently reported. In this section, we will focus on notable HTL materials among reported NPEs. The acidity of PEDOT:PSS, commonly used as HTL in conventional OSCs, causes corrosion of the ITO layer and diffusion of In and Sn from the ITO into the active layer, resulting in the degradation of OSCs over time. A new NPE HTL based on an anionic polystyrene sulfonate (PSS) polyelectrolyte with Cu²⁺ cations has been developed and the interfacial properties between the active layer and new HTLs [Fig. 5(a)] have been investigated.^{40,104,105} The polyelectrolyte possesses neutral pH and the ability to block electrons. Chemical doping has been shown to allow control of the position of the Fermi level in organic semiconductors and to increase the conductivity of organic films, two phenomena that potentially have a significant impact on OSC performance. In this study, mixtures of Cu:PSS and PEDOT:PSS were explored. The experiments using PEDOT:PSS as an additive suggested that mixing 70 μ l of PEDOT:PSS solution with 1 ml of Cu:PSS solution could yield the optimal performance in solar cell devices and have almost the same effect as mixing with much larger amounts of PEDOT:PSS. This solution will be referred to as “Cu:PEDOT:PSS (A).” Among the mixtures

with relatively large amounts of PEDOT:PSS, one with 90% Cu:PSS and 10% PEDOT:PSS solutions was found to yield optimal results. This solution will be referred to as “Cu:PEDOT:PSS (M).” PEDOT:PSS mixtures with Cu:PSS were more efficient than PEDOT:PSS in modifying the interface and achieving efficient hole extraction. As a result, the PCE values were improved from 8.12% with PEDOT:PSS to 9.01% when using the Cu:PEDOT:PSS (M) interlayer. As depicted in Fig. 5(a), the sulfonate moieties constitute immobile and relatively inert anions. The Cu²⁺ ion may accept electrons from the active layer, changing to Cu⁺ and leaving an excess negative charge on the PSS backbone which compensates the resulting positive charges in the active layer near the HTL interface. XPS and UPS were used to develop a detailed understanding of the interfacial energy level alignment, electronic band structure, and band bending (V_b) at the HTL/poly [4,8-bis[(2-ethylhexyl)oxy]benzo [1,2-b:4,5-b']dithiophene-2,6-diy][3-fluoro-2-[(2-ethylhexyl)carbonyl]thieno[3,4-b]thiophenediy] (PTB7) interface. Collecting all the WF, hole injection barrier (ϕ_h), electron injection barrier (ϕ_e), V_b , EA, IP, and the LUMO and HOMO level information revealed changes in the interface formation of ITO/HTLs/PTB7 due to an addition of Cu:PSS. As shown in corresponding energy level diagrams in Fig. 5(b), ϕ_h from donor to HTLs are 0.59 eV for Cu:PSS,

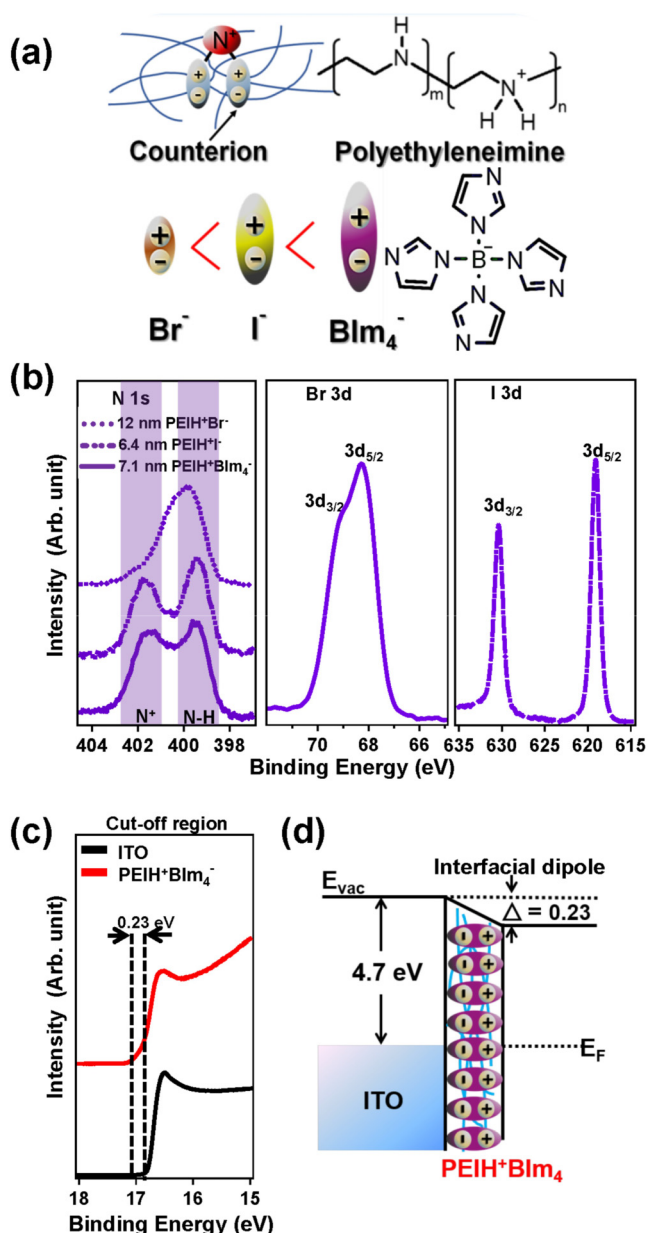


FIG. 4. (a) Chemical structures of NPEs. (b) XPS spectra of N 1s, Br 3d, and I 3d for NPEs. (c) UPS spectra of ITO and ITO/PEIH⁺ Blm_4^- films. (d) Energy level diagram of the inverted OSCs. Reproduced with permission from Kang *et al.*, RSC Adv. **9**, 20670 (2019). Copyright 2019 Royal Society of Chemistry.

0.34 eV for Cu:PEDOT:PSS (A) and 0.17 eV for Cu:PEDOT:PSS (M). Cu:PEDOT:PSS (A) and Cu:PEDOT:PSS (M) strongly attract electrons from the PTB7 donor phase due to their high WF and interfacial dipole at the anode interface. Comparing the data for Cu:PSS against Cu:PEDOT:PSS (A) and Cu:PEDOT:PSS (M) suggests that mixtures of Cu:PSS with PEDOT:PSS result in larger

interfacial dipoles and band bending effects. In addition, an increase in the barrier to electron back diffusion is induced to the maximum value of 1.50 eV for [Cu:PEDOT:PSS (M)/PTB7] and leads to faster extraction of holes and electrons, reduced leakage current, and reduced carrier recombination.

Ternary OPVs that contain a blend of three donor/acceptor component materials have emerged as an effective strategy to combine and fine-tune absorption spectra and energy band structures to produce high-efficiency solar cells, and PES has played an important role in understanding these ternary systems as well. For example, Lami *et al.* in 2020 used UPS and XPS to investigate how ternary mixtures of one donor and two acceptors can be used to tune the energy band structure and control V_{OC} of OPVs and identify the energy losses.¹⁰⁶ Vanadium oxide and PEDOT:PSS are two well-known HTL types that have been shown to work effectively; however, they are not usually used together. Teng *et al.* showed that mixtures of vanadium oxide and PEDOT:PSS could produce better performance (10%–100% relative increase in PCE) upon mixing a vanadium oxide sol-gel precursor with PEDOT:PSS.¹⁰⁷ Chang *et al.* studied the interface between the active layer and reported that cathode in OPVs could be modified with a variety of carrier selective interlayers. They were able to improve the PCE of devices from 1.06% to 4.15%, largely through increased V_{OC} using bathocuproine, which resulted in the best performance compared to other interlayers.¹⁰⁸ As OPVs reach higher efficiencies, their ability to be processed economically and stabilities have become factors which limit their practical application more than electrical parameters. Yin *et al.* employed PES to investigate the effects of air exposure on the electronic properties of solar cells. They discovered that MoO₃ penetrates significantly into the active layer upon thermal evaporation, creating an interface dipole at the anode which decreases upon air-exposure and, in turn, decreasing the device performance.¹⁰⁹

B. Metal oxides (inorganic materials)

Metal oxides have useful physical properties making them suitable for use with organic photovoltaic devices as interfacial layers. In the BHJ structure, they may not only serve as charge selective contacts but also act as electron acceptors. Compared to other interfacial materials, metal oxides offer advantages such as excellent stability, low cost, and desirable electronic properties including high charge carrier mobilities.¹¹⁰ To achieve good ohmic contacts, various metal oxide interlayers have been used between the BHJ layer and the electrodes.⁴⁹ Metal oxides exist in a wide variety of materials and, in particular, transition metal oxides have a wide range of WFs ranging from about 3.0 eV (ZrO_2)¹¹¹ to 7.0 eV (V_2O_5).¹¹² TiO_2 , ZnO , and SnO_2 are frequently used as ETLs, while V_2O_5 , MoO_x , and NiO_x are commonly used as HTLs in OSCs.^{42,113,114} Metal oxides can be selected as interlayer materials based on the alignment of their valence and conduction band edges with the various HOMO and LUMO levels of organic semiconductors.

A growing number of studies have established that solution-processed MoO_x is an excellent HTL in BHJ OSCs and is one of the most effective *p*-type metal oxides. These solution-processed metal oxides, however, have a major impediment; an annealing process at high temperatures is usually required to produce high-

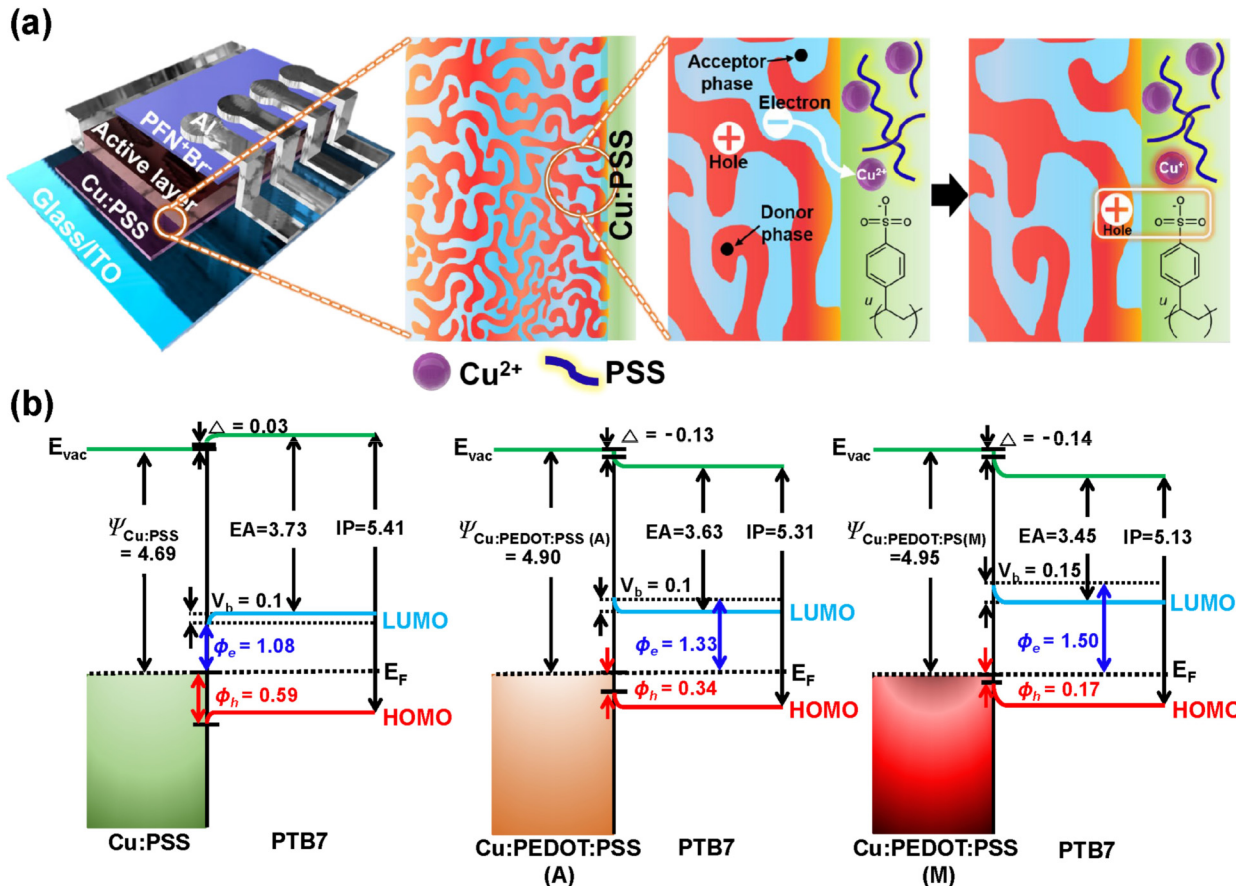


FIG. 5. OSC devices using Cu:PSS as a HTL. (a) Device architecture and schematic diagram showing the p-type doping effect of Cu:PSS. (b) Schematic self-assembly of Cu:PSS films before and after the doping of PEDOT:PSS in Cu:PSS, PTB7 on ITO/Cu:PSS, PTB7 on ITO/Cu:PEDOT:PSS (A) and PTB7 on ITO/Cu:PEDOT:PSS (M). Reproduced with permission from Kang *et al.*, Sol. RRL 5, 2100521 (2021). Copyright 2021 Wiley.

quality metal oxide films.^{115,116} Tran *et al.* reported increased efficiency in solar cells using solution-processed MoO_x which does not require annealing and analyzed its electronic structure.¹¹⁷ Rather than high annealing treatments, aqueous-MoO_x was prepared using an aqueous sol-gel method. This annealing-free solution processable aqueous MoO_x was then applied to BHJ polymer solar cells based on the poly[(2,6-(4,8-bis(5-(2-ethylhexyl-3-fluoro)thiophen-2-yl)-benzo)[1,2-b:4,5-b']dithiophene))-alt-(5,5-[1',3'-di-2-thienyl-5',7'-bis(2-ethylhexyl)benzo[1',2'-c:4',5'-c'] dithiophene-4,8-dione) (PBDB-T-2F): (2,2'-(2Z,2'Z)-((12,13-bis(2-ethylhexyl)-3,9-diundecyl-12,13-dihydro-[1,2,5]thiadiazolo[3,4-e]thieno[2,3'',4',5']thieno[2',3':4,5']pyrrolo[3,2-g]thieno[2',3':4,5']thieno[3,2-b]indole-2,10 diyl)bis(methanlylidene))bis(5,6-difluoro-3-oxo-2,3-dihydro-1H-indene-2,1-diyldiene))dimalononitrile) (Y6). Non-fullerene solar cell made using the anhydrous-MoO_x HTL by the sol-gel process without annealing, exhibited a poor efficiency of 7.7%. The efficiency was improved to 17.1%, when this anhydrous-MoO_x layer was annealed at 200 °C. The aqueous-MoO_x solar cell made by the

sol-gel process, on the other hand, showed 17% efficiency, which is very close to the performance of the annealed-MoO_x HTL without high-temperature treatment. Furthermore, compared to the solar cell utilizing PEDOT:PSS (16.6%), the solar cell using aqueous-MoO_x (17%) demonstrated higher efficiency and improved stability without high-temperature annealing. The WF and ϕ_h values of MoO_x layers prepared by the sol-gel method and other curing methods were measured by UPS and compared in Fig. 6(a). With a 0.4 eV difference between the case without the annealing process (4.74 eV) and the case with the annealing process (5.14 eV), the WF contributed to the dipole creation and the ϕ_h value was reduced by 0.25 eV with the annealing process, making it easier to extract holes. The ϕ_h of aqueous-MoO_x prepared without thermal treatment had an aqueous sol-gel approach of 0.60 eV and the dipole value was similar to that of the sol-gel method requiring annealing. The difference between the annealing procedure and the sol-gel technique was investigated using XPS. The Mo 3d and O 1s XPS spectra are presented

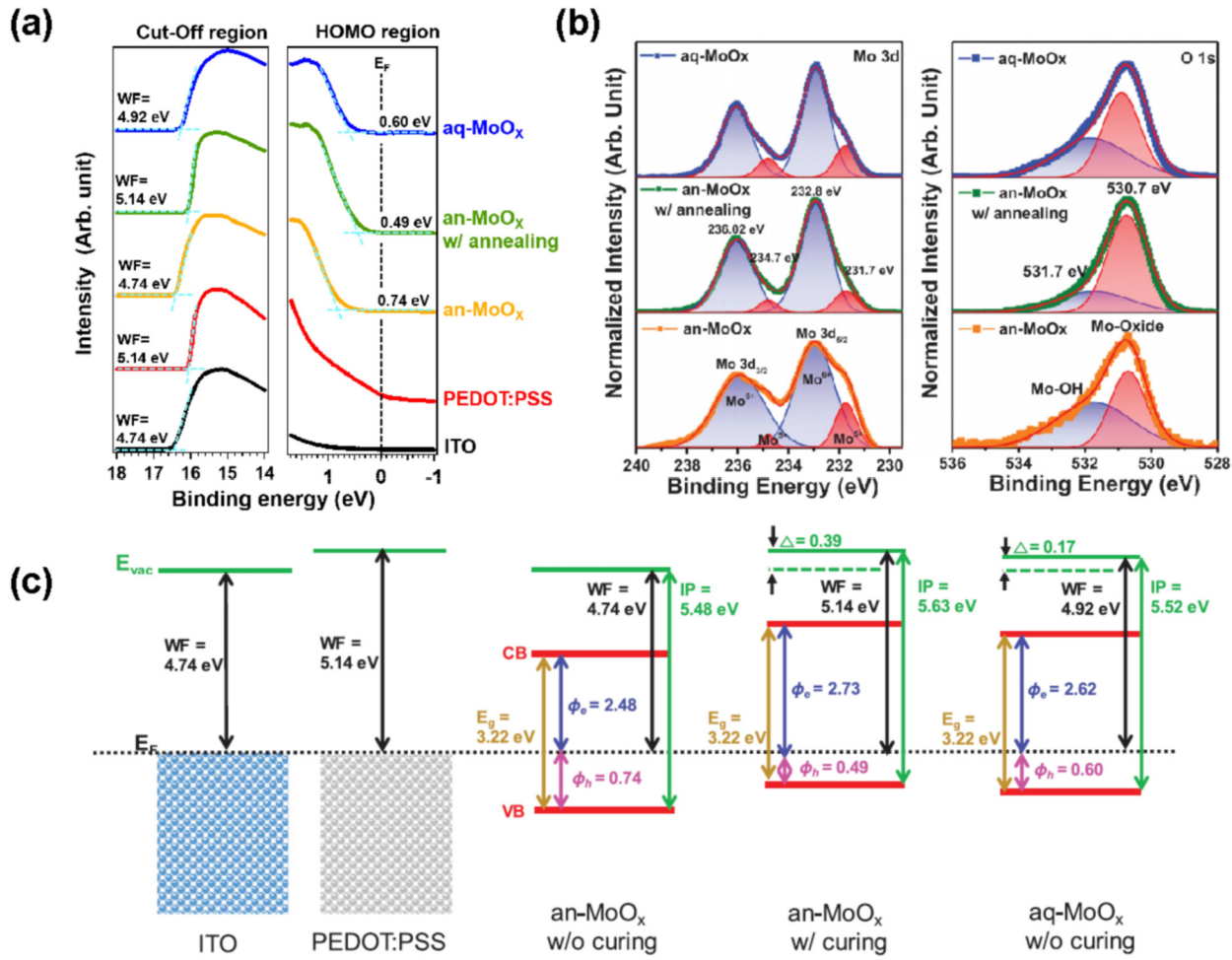


FIG. 6. (a) UPS spectra of MoO_x layers. (b) XPS spectra of Mo 3d and O 1s core level peaks obtained from the MoO_x layers. (c) The energy level diagram of the OSC with a conventional structure and band diagrams of aqueous-MoO_x and anhydrous-MoO_x with and without annealing layers obtained from UPS measurements. Reproduced with permission from Tran *et al.*, *Adv. Sci.* 7, 2002395 (2020). Copyright 2020 Wiley.

in Fig. 6(b). The Mo⁶⁺ oxidation states appear at the binding energies of 232.8 and 236.02 eV, while the Mo⁵⁺ oxidation states have the energies of 231.7 and 234.5 eV. The ratios of the integrated peak areas of each component were used to calculate the atomic concentration ratio of Mo⁶⁺/Mo⁵⁺. Unannealed-MoO_x and aqueous-MoO_x had the Mo⁶⁺/Mo⁵⁺ ratios of 3.86 and 4.59, respectively. The Mo⁶⁺/Mo⁵⁺ ratio was 5.13 with the annealing of anhydrous-MoO_x. In the O 1s spectra, the metal Mo atom is linked to the lower E_b O 1s peak (oxygen-LBE) at 530.7 eV, while the acetylacetone ligand is linked to the O 1s peak (oxygen-HBE) at a higher E_b of 531.7 eV. The oxygen-HBE/oxygen-LBE ratios for anhydrous-MoO_x (without annealing), anhydrous-MoO_x (annealing), and aqueous-MoO_x were 1.28, 0.41, and 0.94, respectively. Compared to unannealed anhydrous-MoO_x, annealed anhydrous-MoO_x had a greater Mo⁶⁺/Mo⁵⁺ ratio and a lower oxygen-HBE/oxygen-LBE ratio. The breakdown of acetylacetone ligand resulted in additional

oxidation of Mo⁵⁺ to Mo⁶⁺ according to these results. In three MoO_x HTLs, the degradation of acetylacetone ligands follows a similar tendency to the efficiency of solar cells. The UPS analysis is summarized in Fig. 6(c) as a band diagram. On the ITO surface, E_F was computed and all other spectra were shown in proportion to this value. The computed E_F values for ITO and PEDOT:PSS were 4.74 and 5.14 eV, respectively. For unannealed anhydrous-MoO_x HTL, anhydrous-MoO_x HTL with annealing, and aqueous-MoO_x, the WF values and inferred h values were 0.74, 0.49, and 0.60 eV, respectively. The performance of polymer solar cells is heavily influenced by this change in the energy level. This difference was consistent across all solar cell measurements.]Just as MoO_x is well known as an HTL, ZnO is a frequently used ETL that has long been known as an effective *n*-type semiconductor and utilized throughout the development of OSCs. For example, ZnO was one of the first materials to be demonstrated as an effective *n*-type substrate for

inverted solar cell devices.^{118–120} Recently, Upama *et al.* investigated the surface properties of ZnO films and nanoparticles (NPs).¹²¹ Using different ZnO fabrication processes, four types of ETL were created. The efficiencies of BHJ inverted structure solar cells using ZnO, double layer sol-gel ZnO (DZO), ZnO-NP, and double-layer ETLs with four ETLs in poly[(2,6-(4,8-bis(5-(2-ethylhexyl)thiophen-2-yl)-benzo[1,2-b:4,5-b']dithiophene))-alt-(5,5-[1',3'-di-2-thienyl-5',7'-bis(2-ethylhexyl)benzo[1',2'-c:4',5'-c']dithiophene-4,8-dione)] (PBDB-T) : 3,9-bis(2-methylene-(3-(1,1-dicyanomethylene)-indanone))-5,5,11,11-tetrakis(4-hexylphenyl)-dithieno[2,3-d:2',3'-d']-s-indaceno[1,2-b:5,6-b']dithiophene (ITIC) were 10.6%, 11.11%, 11.21%, and 12.24%, respectively. Compared to a control device employing solely ZnO as an ETL, the device with the dual interlayer showed improved PCE. Figure 7(a) shows the evolution of secondary electronic edges for various ETLs extracted from UPS spectra. The WFs were found to be 4.16, 4.08, 4.04, and 4.04 eV for ZnO, double layer sol-gel ZnO (DZO), ZnO-NP, and double-layer ETL, respectively. The energy level structures of the ITO/ZnO cathode and ITIC acceptor with and without a ZnO-NP layer are depicted in Fig. 7(b). When ZnO-NPs

are deposited between ITO and ZnO [right diagram in Fig. 7(b)], the interfacial energy barrier for electrons is lowered, facilitating the electron transport from ITIC to the ETL. As a result, improved electron transport was observed and the efficiency of the bilayer device was improved. Also, the presence of fewer chemisorbed surface species in the ETL was observed from XPS measurements, indicating the potential for enhanced conductivity and electron mobility in the ETL as presented in Fig. 7(c). In general, the sub-peaks O1s A, O1s B, and O1s C in the ZnO film correspond to chemical bonds (Zn–O bonds), oxygen vacancies, and bonds between adjacent zinc and oxygen atoms, respectively.^{122,123} Oxygen vacancies are known to act as recombination centers for photogenerated holes and electrons, lowering FF and PCE. In addition, Li *et al.*, have shown that surface hydroxide and the presence of zinc and oxygen vacancies may act to increase the WF of ZnO.¹²⁴ The relatively low oxygen vacancies of ZnO-NPs may lead to a decrease in the WF observed in UPS measurements.

TiO_x like ZnO is a well-known *n*-type semiconductor that has been widely employed in OSCs.^{125,126} TiO_x can operate as a photocatalyst by absorbing light in the UV area due to its relatively large

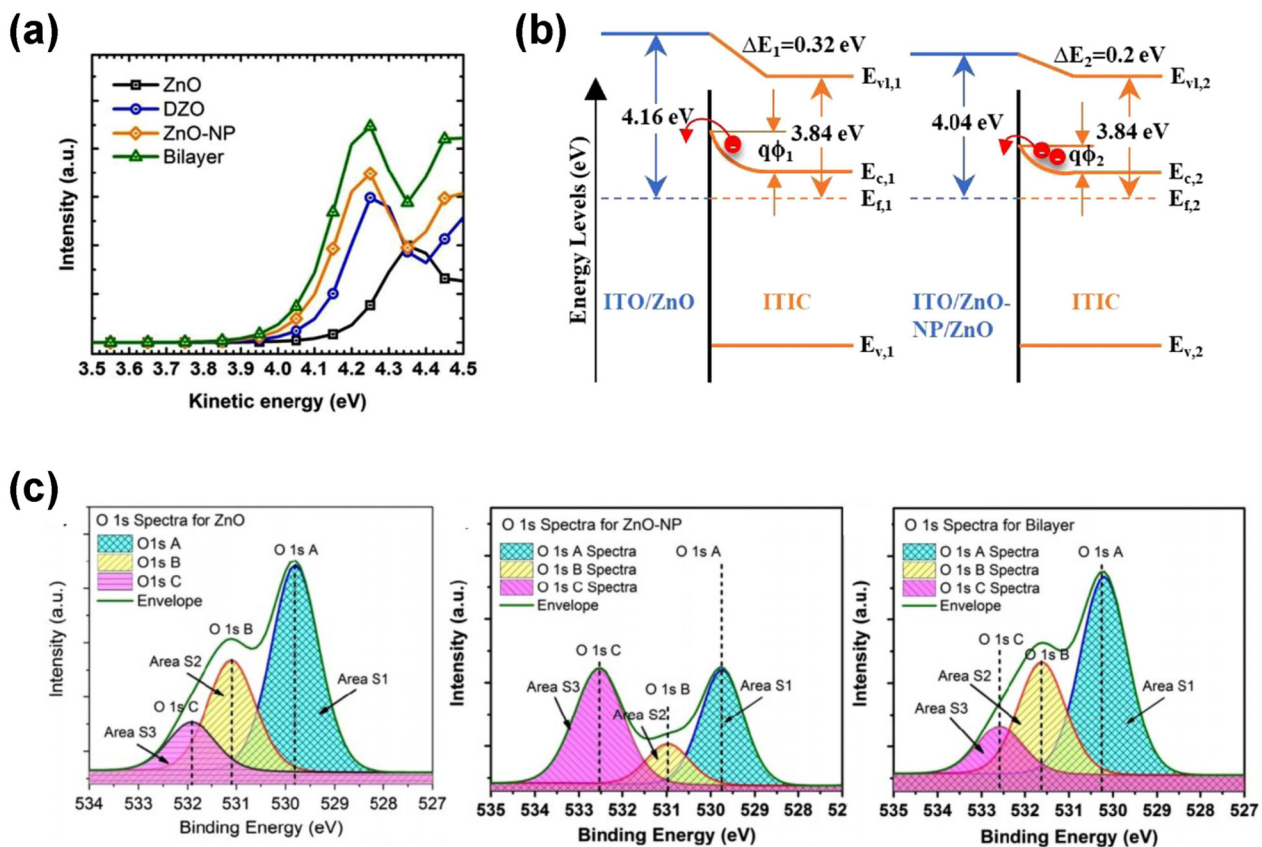


FIG. 7. (a) Secondary electron edge for different ETL films on the ITO/glass substrate from UPS measurement. (b) Energy level alignments of ITO/ETL/ITIC, depicting the band bending phenomenon. (c) O 1s XPS spectra for ZnO, ZnO-NP and bilayer ETL. Reproduced with permission from Upama *et al.*, Energy Mater. Sol. Cells **187**, 273 (2018). Copyright 2018 Elsevier.

bandgap of 3.0–3.2 eV.¹²⁷ Amelot *et al.* investigated the interface between fullerene acceptors and low-temperature sputtered TiO_x.¹²⁸ Using enhanced PES, they proposed a complete explanation for the electronic interactions at the interface between TiO_x and C₇₀ fullerene molecules. To better understand the modification of the electronic structure at the C₇₀/TiO_x interface, Ti L_{3,2} XAS spectra were investigated for clean TiO_x and TiO_x with thin layers of C₇₀ and the results are shown in Fig. 8(a). Weak differences were observed at the Ti L_{3,2} edges before and after the deposition of 0.65 nm of C₇₀, indicating that vacant Ti orbitals are weakly influenced by the molecules. The C 1s electron binding energies determined from XPS spectra reflect nearly identical band bending values for TiO_x sputtered at 150 and 350 °C [Fig. 8(b)]. Both show downward band bending of about 0.1 eV from the C₇₀ IUMO to the TiO_x conduction band, indicating favorable electron transfer from the C₇₀ IUMO to the TiO_x conduction band. Based on the spectroscopic results, detailed energy band diagrams were drawn from the interface as shown in Fig. 8(c). The ϕ_e value for TiO_x is 0.1 eV and C₇₀ has a larger value of 0.3 eV, suggesting that electron extraction is favorable compared to hole extraction. This interfacial state is expected to support the favorable energy band alignment observed, showing a perfect match of transport levels for barrier-free extraction of charges and making the sputtered TiO_x layers good ETL candidates at the interface with fullerene acceptors in OSCs. In 2020, Thambidurai *et al.* examined the effect of gallium doping on the electronic band structure of TiO₂ ETLs by UPS and XPS, and they were able to improve the PCE from 6.65% to 7.72% using this strategy.¹²⁹ Despite not being a metal oxide technically, copper thiocyanate (CuSCN) is an inorganic material that has recently emerged as an effective HTL in both perovskite and OPV devices. Odeke *et al.* investigated the electronic band structure of CuSCN HTLs using PES and showed that dimethyl sulfoxide solvent molecules interact with the material and have a desirable stabilizing effect on the band structure, explaining its good performance.¹³⁰ Copper oxide has long been known as a *p*-type semiconductor, however, relatively few reports have addressed the possibility of solution-processing this material in the context of OPVs. Patel *et al.* used PES to study the properties of CuO thin films prepared by spincoating and annealing copper acetate solutions, and reported the improvement in photocurrent generation relative to a PEDOT:PSS control.¹³¹

C. Inorganic–organic materials (hybrid materials)

With further development of thin-film organic molecular strategies, a novel organic–inorganic hybrid interlayer has recently emerged as new focus of research in this field and several significant advances have been made in its applications to solar cells. Inorganic semiconductors exhibit extended band states and high charge carrier mobility, and can generate a large density of electron-hole pairs by electrical injection. For example, there are reports of improved efficiency and stability in inverted OSCs via introduction of a ZnO-PFN interlayer.¹³² ZnO/PFN hybrid interlayers with a hydrophobic surface were deposited on top of the ITO electrode and the ZnO surface defects were reduced through modification of their chemical composition. The ZnO-PFN interlayer overcomes the disadvantages of conventional hydrophilic ZnO

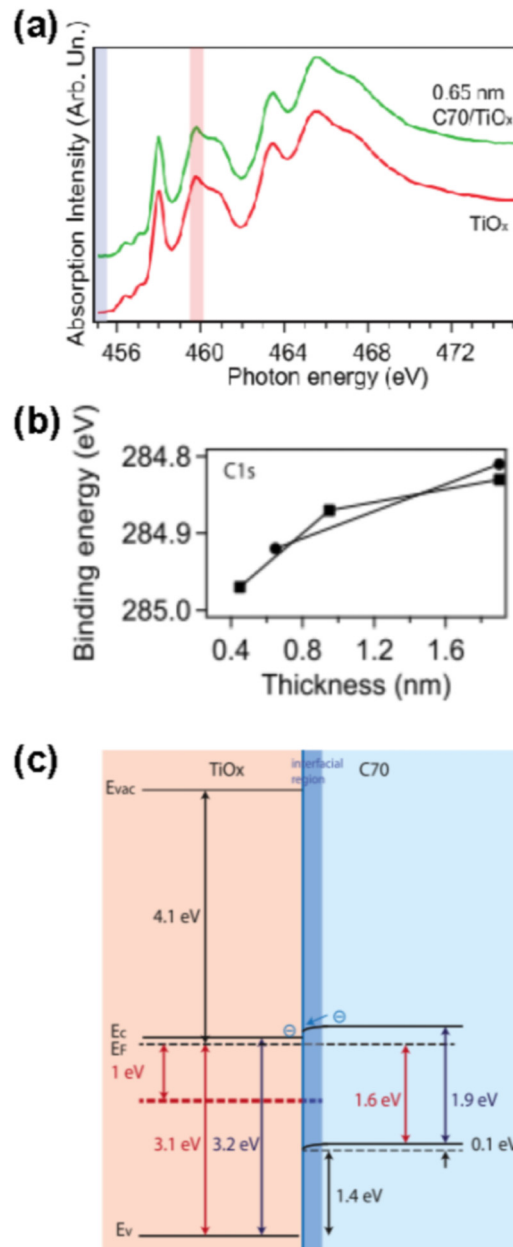


FIG. 8. (a) Absorption at Ti L_{3,2} edge (2p-3d). (b) Variation of E_b of C 1s vs C₇₀ thickness for TiO_x sputtered at 150 °C (circle) and TiO_x sputtered at 350 °C (square). (c) Band diagrams of C₇₀/TiO_x as derived from the photoemission spectra. Reproduced with permission from Amelot *et al.*, ACS Appl. Mater. Interfaces 13, 19460 (2021). Copyright 2021 Elsevier.

surface due to the characteristics of conjugated polymer (PFN), which improves interaction with organic active layers. While above example uses a bi-layer structure, there are also reports on effective interlayers consisting of ZnO and CPEs mixed in a single

layer.^{133–136} These interlayers are composed of hybrid materials synthesized from corresponding organic and inorganic components, thus combining the advantages of two components such as good conductivity and organic compatibility.^{137–139} These studies again demonstrate that inserting an appropriate interlayer containing dipoles between inorganic and organic layers is an effective way to shift the electrostatic potential at the interface favoring charge carrier extraction and is a natural way to tune the energy level alignment of semiconductors.

Due to its high conductivity, graphene has drawn substantial interest as high performance transistor materials and transparent conductive electrodes for some time.^{140–142} An OSC architecture using a graphene/Cu bilayer as an anode electrode instead of ITO

has been reported while taking advantage of the properties of graphene.⁵⁸ Using a BHJ active layer mixture of PTB7: [6,6]-phenyl-C₇₁-butyric acid methyl ester (PC₇₁BM), the efficiency of solar cells using single graphene layers was 2.98%, while the efficiency of double layer with an additional 3 nm Cu layer was 4.12%. Although the efficiency is low compared to that of the widely used ITO electrode, this work demonstrates that this new electrode can be utilized to make functioning OSCs from abundant materials, which may have the potential to replace ITO in future. XPS and UPS measurements were used to determine the electronic properties of the electrode. The change in the WF of graphene with various thicknesses of inorganic Cu layer on graphene was quantified through UPS as shown in Fig. 9(a). The WF increased from

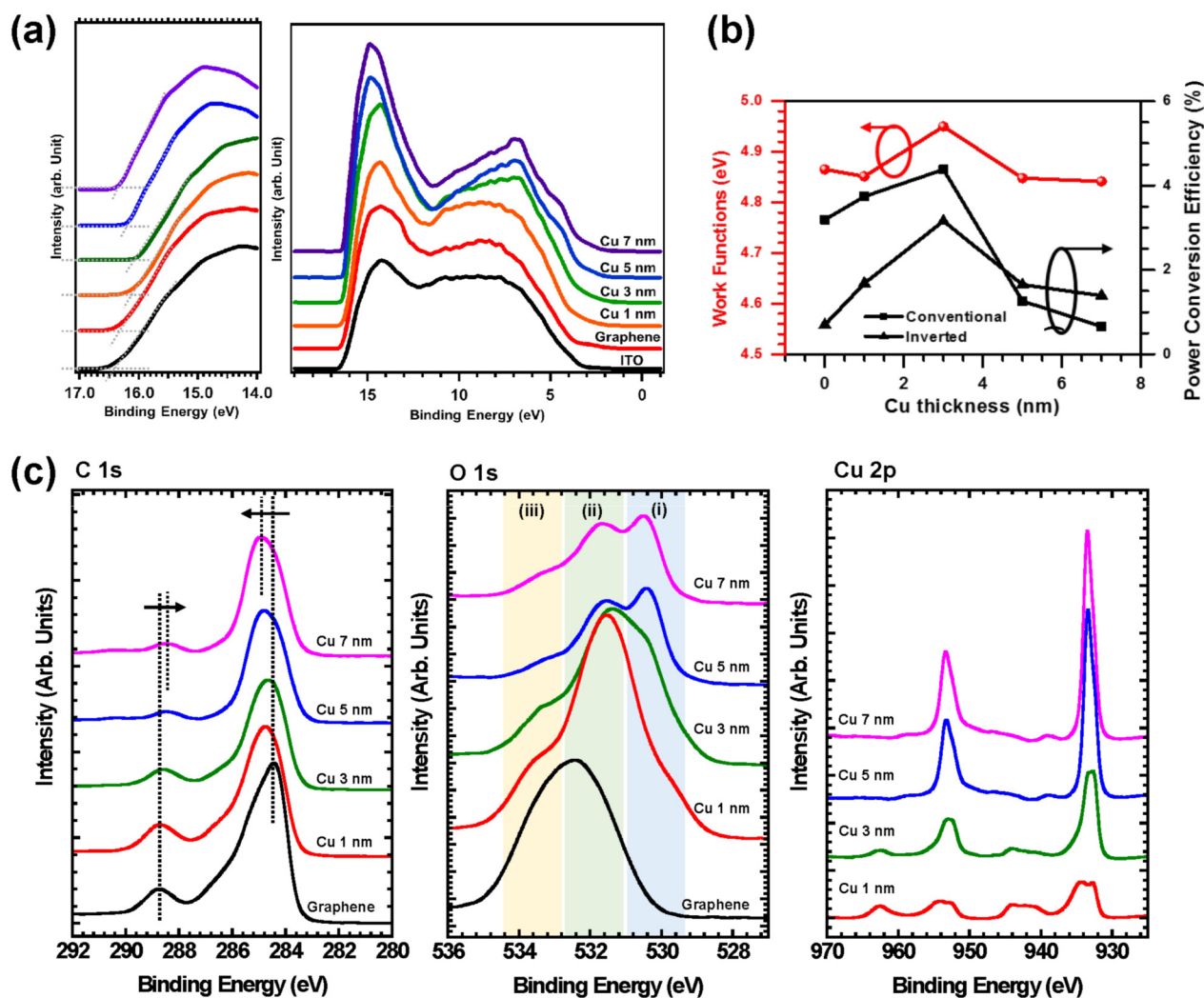


FIG. 9. (a) Cut-off region and UPS full spectra of Cu/graphene hybrid sheets as a function of Cu thicknesses. (b) WFs and power conversion efficiencies vs Cu/graphene hybrid sheets. (c) XPS spectra of C 1s, O 1s, and Cu 2p of the graphene surface as a function of the Cu film thicknesses. Reproduced with permission from Kang *et al.*, Carbon 171, 341 (2021). Copyright 2021 Elsevier.

4.87 eV for pristine graphene to 4.95 eV as the thickness of Cu layer increased from 0 to 3 nm. However, with further increase in the Cu-layer thickness, the WF decreased [Fig. 9(b)]. The chemical interaction in Cu/graphene hybrid sheets was investigated by XPS and the XPS spectra of C 1s, O 1s, and Cu 2p core levels are presented in Fig. 9(c). The C 1s spectra are typical of graphene oxide. In the peak fitting of O 1s, there are two spectral features in the regions near 530 eV [CuO region (i)] and 531.5 eV [Cu₂O region

(ii)] as the Cu thickness increases. Changes in these spectral features suggest that the oxygen adsorption rate of Cu₂O decreases [region (ii)] and the metal Cu proportion increases [region (i)]. The results can also be confirmed in Cu 2p XPS spectra. The appearance of CuO appears at the beginning of Cu deposition, but as the thickness increases, the shape of the spectrum gradually resembles that of metallic Cu. Having sufficiently thick Cu layer on graphene, the advantages of low surface resistance and high

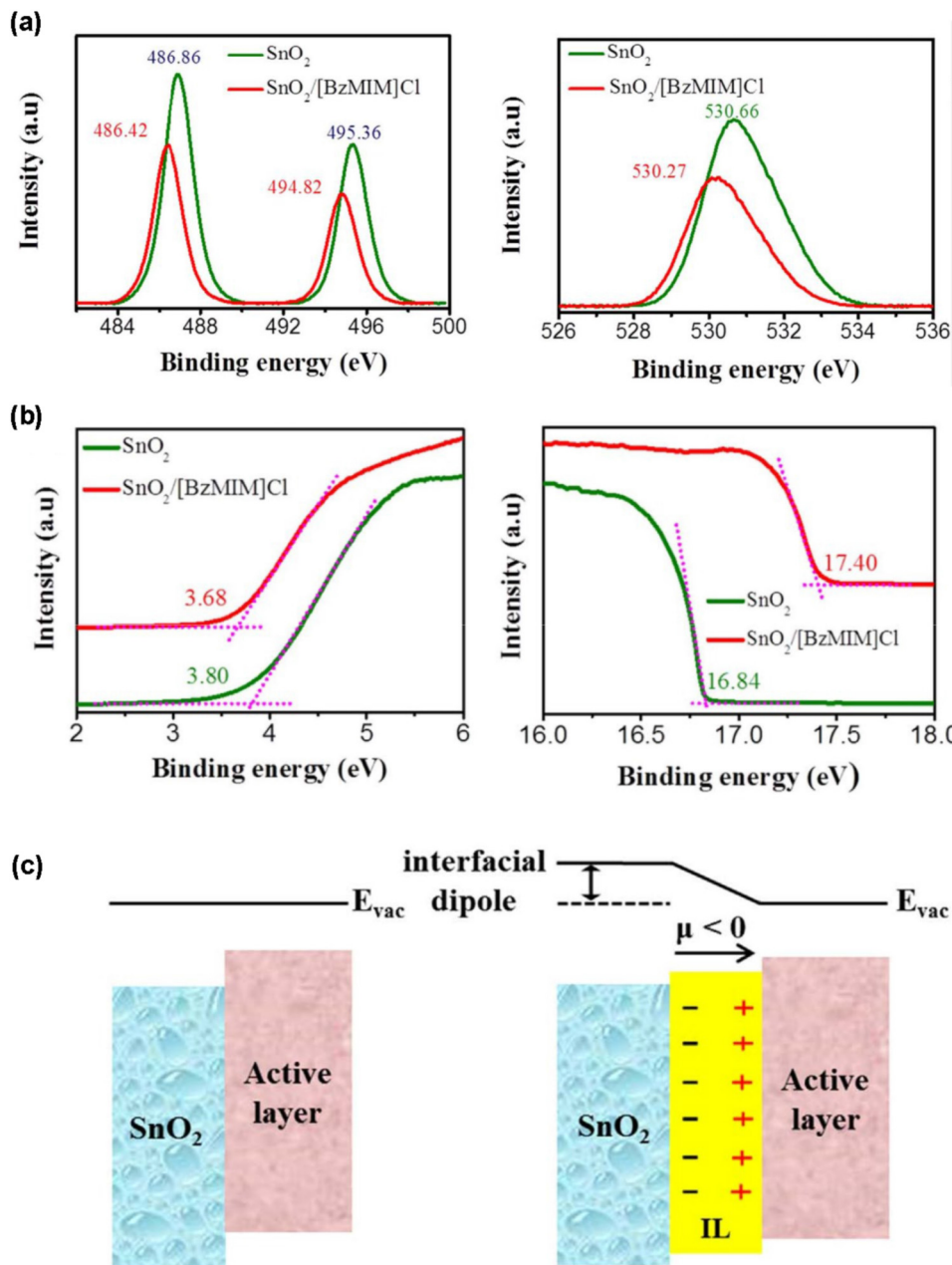


FIG. 10. (a) UPS spectra of SnO₂ and SnO₂/[BzMIM]Cl films; valence region and secondary electron cutoff. (b) SnO₂ and SnO₂/[BzMIM]Cl films XPS spectra of Sn 3d and O 1s. (c) Schematic for vacuum level shift and reduced work function of ITO/SnO₂ after coating with [BzMIM]Cl. Reproduced with permission from Tran *et al.*, Sol. Energy Mater. Sol. Cells **179**, 260 (2018). Copyright 2018 Elsevier.

conductivity of Cu could be combined with high transparency of graphene and it would enable low-cost, hybrid electrodes with excellent potential for replacement of ITO and applications to new areas.

One branch of ETL research has recently focused on the development of SnO_2 as an ETL for optoelectronic devices due to its attractive features such as high optical transparency, suitable band energies, and high electron mobility.¹⁴³ For example, Tran *et al.* reported a low temperature solution-treated combination of an ionic liquid (IL) and SnO_2 , which was able to create an ohmic contact between the ETL and the photoactive layer.¹⁴⁴ "Solid state" ILs are known for their unique physicochemical properties including high electrical conductivity, high carrier mobility,¹⁴⁵ good thermal stability,¹⁴⁶ etc., have been widely used in batteries, supercapacitors, actuators, and OSCs.^{147,148} Using 1-benzyl-3-methylimidazolium chloride ([BzMIM]Cl) as an IL, it was shown to function as an ETL and to enable high efficiency OSCs. The efficiency of P3HT:

PC_{61}BM OSC devices was found to be 2.94% when using a single layer of SnO_2 . However, by employing a double layer structure of SnO_2 and IL was used, the efficiency could increase to 4.05%. XPS was used to determine the surface composition and chemical states in the SnO_2 and SnO_2/IL ETLs [Fig. 10(a)]. High-resolution XPS spectra for Sn and O region of SnO_2 (green lines) show strong peaks at 486.86, 495.36, and 530.66 eV, which correspond to Sn 3d_{5/2}, Sn 3d_{3/2}, and O 1s states of SnO_2 , respectively. The Sn3d_{5/2}, Sn3d_{3/2}, and O 1s binding energies are decreased to 486.42, 494.82, and 530.27 eV for SnO_2/IL (red lines), respectively. The impact of electronegative Cl^- anion coordinating to Sn causes these shifts in the Sn and O XPS spectra. On the other hand, the UPS spectra for SnO_2/IL ETLs reveal that the WF at the cathode is dramatically decreased from 4.38 to 3.82 eV, as illustrated in Fig. 10(b). The valence onset of SnO_2 was measured at 3.80 eV, while that of SnO_2/IL was measured at 3.68 eV, indicating a small drop in ϕ_b . Because of the vacuum level shift, the bi-layered SnO_2/IL ETL was

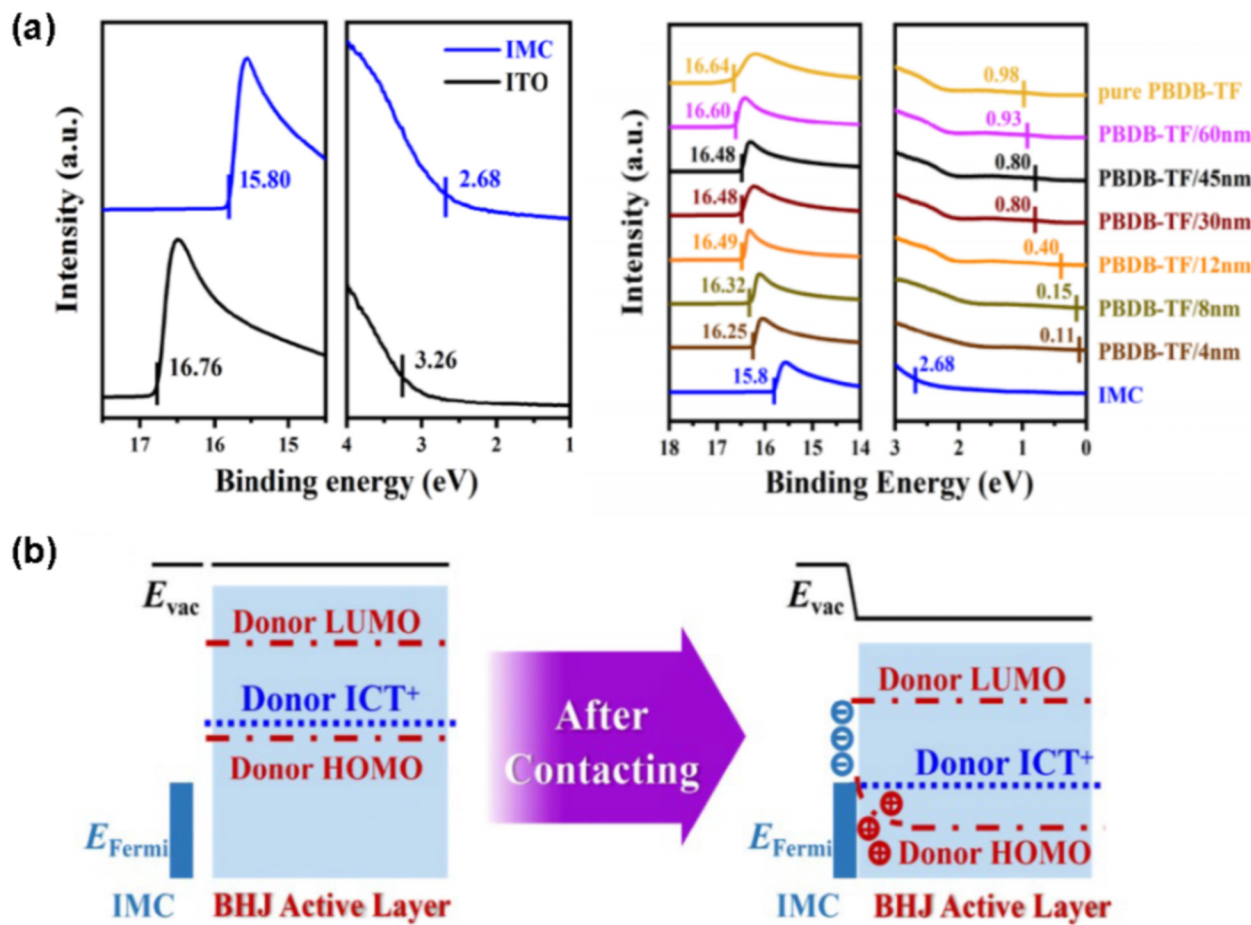


FIG. 11. (a) Structure of the Dawson-type IMC. (b) UPS spectra of ITO, IMC, and PBDB-TF on the IMC with various thicknesses. (c) Interfacial energy diagram of the PBDB-TF/IMC interface. Reproduced with permission from Yang *et al.*, ACS Appl. Mater. Interfaces **12**, 39462 (2020). Copyright 2020 American Chemical Society.

superior in creating an ohmic contact between the ETL and the photoactive layer rather compared to single-layer SnO₂ [Fig. 10(c)].

Dual-layer hybrid structures of inorganic and organic materials sometime have the disadvantage of being difficult to fabricate, unstable, and prone to defect states due to mismatched solid-state structures and surface properties. However, solution-processed materials that blend organic and inorganic components have been developed using single-layer structures rather than a double-layer one. For example, Yang created high-efficiency large area OSCs using inorganic molecular clusters (IMCs) as an HTL.¹⁴⁹ IMC materials have several benefits, including a neutral pH, high light transmittance, high WF, good film-forming properties, and low cost. Poly[4,8-bis[5-(2-ethylhexyl)-4-fluoro-2-thienyl]benzo-[1,2-b:4,5-b']dithiophene-2,6-diyl]-2,5-thiophenediy - [57-bis(2-ethylhexyl)-4,8-dioxo-4H,8H-benzo[1,2-c:4,5-c']- dithiophene-1,3-diyl]-2,5-thiophenediy] (PBDB-TF): 2,2'-[6,6,12,12-Tetrakis(4-hexylphenyl)-6,12-dihydrodithieno[2,3-d:2',3'-d']-s-indaceno[1,2-b:5,6-b'] dithiophene-2,8-diyl]bis[methyldyne(5,6-difluoro-3-oxo-1H-indene-2,1(3H)-diylidene)]bis[propanedinitrile] (IT-4F) BHJ devices were created with PEDOT:PSS and IMC HTLs, and their characteristics were compared. PEDOT:PSS is a widely used benchmark HTL and showed 13.10% of PCE, whereas the devices using IMCs reached 13.38%. Although the increase in PCE was not significant, there are very few examples of HTLs which are solution-processable and pH-neutral at the same time as being more efficient than PEDOT:PSS. Using UPS for the properties of HTLs, the WF of ITO substrate was determined to be 4.32 eV and increased to 5.28 eV by covering it with the IMC layer [Fig. 11(a)]. In addition, to take account for the energy level alignment at the IMC/active layer interface, IMC:PBDB-TF bilayers with different PBDB-TF film thicknesses were prepared and the surface WF of the bilayer was measured by UPS. As shown in Fig. 11(b), the WF of pure IMC film was found to be 5.28 eV. After depositing an ultra-thin (4 nm) PBDB-TF film, it decreased to 5.22 eV, indicating that the vacuum level shifted downward due to the interfacial dipole created by the interfacial layer. When the PBDB-TF thickness was increased to 8 nm, the surface WF of the bilayer decreased to 4.99 eV, approaching the Fermi level of the native polymer PBDB-TF. These results reveal that the region where the energy level alignment is affected by the interfacial dipoles can extend beyond 8 nm into the active layer. Moreover, when the PBDB-TF thickness continued to increase beyond 15 nm, the surface WF dropped to 4.60 eV and slowly approached the intrinsic Fermi level of PBDBTF with further increase in PBDB-TF thickness. Moreover, it was observed that the HOMO of PBDB-TF shifted closer to the Fermi level at the IMC/PBDB-TF interface, which is consistent with the observation of Fermi pinning, where electron transfer from polymer to IMC occurs. The change in vacuum level implied the formation of interfacial dipoles from PBDB-TF to IMC. The band bending can also be seen in UPS results. The IP of the ultra-thin PBDB-TF deposited on IMCs was found to be 5.43 eV which is higher than that of bulk polymer (IP, PBDB-TF = 5.56 eV). Thus, band bending at the interface favors the hole extraction. The findings of this study suggest that the IMC IL is not only effective at optimizing the anode energy band structure for high-efficiency OSC manufacturing but that IMC is also compatible with printing process technology, making it attractive for OSC commercialization.

V. SUMMARY AND OUTLOOK

Interfacial engineering using photoelectron spectroscopy can provide an understanding of the energy level alignment at semiconductor junctions, especially at anode and cathode interfaces inside devices, providing valuable insight and strategies for the development of high-performance OSCs. All the sequential processes of exciton dissociation via photoinduced charge transfer between donors and acceptors, charge transport and collection influence the device characteristics of OSCs. To a large extent, the increase in OSC efficiencies over time have been due to advancements in the understanding of device architectures and materials; in particular, the ability to control band structures at organic/metal interfaces, organic/semiconductor interfaces, and electrode/organic interfaces.

In this review, we have introduced the principles of OSC operation; explained how photoelectron spectroscopy can probe the energy level alignment and electronic structure of the interfaces between ionic and electrolytic thin films, metal oxides, and hybrid materials; and introduced how the electronic band structure of these interfaces affects the device characteristics of OSCs. Understanding the energy level alignment inside a device is critical for the creation of high-performance OSCs and for the continued progress in this field. Photoelectron spectroscopy is unique in this regard as it measures the relevant electronic properties of materials in solid-state thin films under similar conditions that exist in functioning OSC devices.

To achieve high-performance OSCs, interface engineering, aided by the information provided using photoelectron spectroscopy, would substantially contribute to control energy level alignment, improve electron and hole extraction, passivate charge trap states, guide active layer morphology, improve materials compatibility, and change the WF of both anode and cathode electrodes for the optimization of open-circuit voltage, fill factor, and short circuit current density. Interface engineering at organic/metal interfaces, organic/semiconductor interfaces, and electrode/organic interfaces will continue to play a critical role in the future development of OSCs through optimizing the performance and stability of organic multilayer optoelectronic devices. A comprehensive understanding of physics in exciton dissociation and charge transport, together with the knowledge of electronic properties of different interfacial materials and how different combinations of materials influence electronic band structure, would help speed up the development and commercialization of low-cost and high-efficiency OSCs.

ACKNOWLEDGMENTS

This research was supported by the National Research Foundation of Korea (Nos. NRF-2019K1A3A7A09101449, NRF-2020R1F1A1075539, and NRF-2021R1C1C2011757) and the Natural Sciences and Engineering Research Council of Canada (NSERC) (No. RGPIN-2016-04793).

AUTHOR DECLARATIONS

Conflict of Interest

The authors have no conflicts to disclose.

Author Contributions

Ju Hwan Kang: Writing – original draft (lead). **Jin Hee Lee:** Visualization (equal); Writing – original draft (supporting). **Bright Walker:** Writing – review and editing (supporting). **Jung Hwa Seo:** Conceptualization (equal); Funding acquisition (equal); Investigation (equal); Supervision (equal); Writing – review and editing (equal). **Gap Soo Chang:** Conceptualization (equal); Supervision (equal); Validation (equal); Writing – review and editing (equal).

DATA AVAILABILITY

The data that support the findings of this study are available within the article.

REFERENCES

- ¹J. Wan, X. Xu, G. Zhang, Y. Li, K. Feng, and Q. Peng, *Energy Environ. Sci.* **10**, 1739 (2017).
- ²S. Lee, D. Jeong, C. Kim, C. Lee, H. Kang, H. Y. Woo, and B. J. Kim, *ACS Nano* **14**, 14493 (2020).
- ³J. Zhang, H. S. Tan, X. Guo, A. Facchetti, and H. Yan, *Nat. Energy* **3**, 720 (2018).
- ⁴S. D. Dimitrov and J. R. Durrant, *Chem. Mater.* **26**, 616 (2014).
- ⁵E. Zhou, J. Cong, K. Hashimoto, and K. Tajima, *Adv. Mater.* **25**, 6991 (2013).
- ⁶J. Min, Y. N. Luponosov, C. Cui, B. Kan, H. Chen, X. Wan, Y. Chen, S. A. Ponomarenko, Y. Li, and C. J. Brabec, *Adv. Energy Mater.* **7**, 1700465 (2017).
- ⁷X. Che, Y. Li, Y. Qu, and S. R. Forrest, *Nat. Energy* **3**, 422 (2018).
- ⁸Y. Zang, C. Z. Li, C. C. Chueh, S. T. Williams, W. Jiang, Z. H. Wang, J. S. Yu, and A. K. Y. Jen, *Adv. Mater.* **26**, 5708 (2014).
- ⁹R. Xue, J. Zhang, Y. Li, and Y. Li, *Small* **14**, 1801793 (2018).
- ¹⁰Y. Zhu, A. Gadisa, Z. Peng, M. Ghasemi, L. Ye, Z. Xu, S. Zhao, and H. Ade, *Adv. Energy Mater.* **9**, 1900376 (2019).
- ¹¹G. Han and Y. Yi, *Adv. Theory Simul.* **1**, 1800091 (2018).
- ¹²J. Zhang, L. Zhu, and Z. Wei, *Small Methods* **1**, 1700258 (2017).
- ¹³F. Liu, Y. Gu, X. Shen, S. Ferdous, H. W. Wang, and T. P. Russell, *Prog. Polym. Sci.* **38**, 1990 (2013).
- ¹⁴J. C. Aguirre, S. A. Hawks, A. S. Ferreira, P. Yee, S. Subramaniyan, S. A. Jenekhe, S. H. Tolbert, and B. J. Schwartz, *Adv. Energy Mater.* **5**, 1402020 (2015).
- ¹⁵M. Zhang, L. Zhu, G. Zhou, T. Hao, C. Qiu, Z. Zhao, Q. Hu, B. W. Larson, H. Zhu, Z. Ma, Z. Tang, W. Feng, Y. Zhang, T. P. Russell, and F. Liu, *Nat. Commun.* **12**, 309 (2021).
- ¹⁶Z. Zhou, W. Liu, G. Zhou, M. Zhang, D. Qian, J. Zhang, S. Chen, S. Xu, C. Yang, F. Gao, H. Zhu, F. Liu, and X. Zhu, *Adv. Mater.* **32**, 1906324 (2020).
- ¹⁷B. P. Lyons, N. Clarke, and C. Groves, *Energy Environ. Sci.* **5**, 7657 (2012).
- ¹⁸N. Gasparini, F. V. A. Camargo, S. Fröhwald, T. Nagahara, A. Classen, S. Roland, A. Wadsworth, V. G. Gregoriou, C. L. Chochos, D. Neher, M. Salvador, D. Baran, I. McCulloch, A. Görling, L. Lüer, G. Cerullo, and C. J. Brabec, *Nat. Commun.* **12**, 1 (2021).
- ¹⁹K. Schmidt, C. J. Tassone, J. R. Niskala, A. T. Yiu, O. P. Lee, T. M. Weiss, C. Wang, J. M. J. Fréchet, P. M. Beaujuge, and M. F. Toney, *Adv. Mater.* **26**, 300 (2014).
- ²⁰L. Lu, T. Zheng, T. Xu, D. Zhao, and L. Yu, *Chem. Mater.* **27**, 537 (2015).
- ²¹X. Liu, Y. Yan, A. Honarfar, Y. Yao, K. Zheng, and Z. Liang, *Adv. Sci.* **6**, 1802103 (2019).
- ²²L. Nian, K. Gao, F. Liu, Y. Kan, X. Jiang, L. Liu, Z. Xie, X. Peng, T. P. Russell, and Y. Ma, *Adv. Mater.* **28**, 8184 (2016).
- ²³N. Hirata, J. E. Kroese, T. Park, D. Jones, S. A. Haque, A. B. Holmes, and J. R. Durrant, *Chem. Commun.* **5**, 535 (2006).
- ²⁴M. Graetzel, R. A. J. Janssen, D. B. Mitzi, and E. H. Sargent, *Nature* **488**, 304 (2012).
- ²⁵J. T. Shieh, C. H. Liu, H. F. Meng, S. R. Tseng, Y. C. Chao, and S. F. Horng, *J. Appl. Phys.* **107**, 084503 (2010).
- ²⁶Z. A. Page, Y. Liu, V. V. Duzhko, T. P. Russell, and T. Emrick, *Science* **346**, 441 (2014).
- ²⁷B. A. MacLeod, N. E. Horwitz, E. L. Ratcliff, J. L. Jenkins, N. R. Armstrong, A. J. Giordano, P. J. Hotchkiss, S. R. Marder, C. T. Campbell, and D. S. Ginger, *J. Phys. Chem. Lett.* **3**, 1202 (2012).
- ²⁸T. H. Lai, S. W. Tsang, J. R. Manders, S. Chen, and F. So, *Mater. Today* **16**, 424 (2013).
- ²⁹B. A. Gregg and M. C. Hanna, *J. Appl. Phys.* **93**, 3605 (2003).
- ³⁰Y. Zhu, T. Song, F. Zhang, S. T. Lee, and B. Sun, *Appl. Phys. Lett.* **102**, 113504 (2013).
- ³¹N. Tessler, *J. Appl. Phys.* **118**, 215501 (2015).
- ³²Y. Wang, J. Han, L. Cai, N. Li, Z. Li, and F. Zhu, *J. Mater. Chem. A* **8**, 21255 (2020).
- ³³J. H. Seo, A. Gutacker, Y. Sun, H. Wu, F. Huang, Y. Cao, U. Scherf, A. J. Heeger, and G. C. Bazan, *J. Am. Chem. Soc.* **133**, 8416 (2011).
- ³⁴K. Yuan, L. Chen, and Y. Chen, *J. Phys. Chem. B* **118**, 11563 (2014).
- ³⁵G. E. Lim, Y. E. Ha, M. Y. Jo, J. Park, Y. C. Kang, and J. H. Kim, *ACS Appl. Mater. Interfaces* **5**, 6508 (2013).
- ³⁶J. H. Kang, Y. J. Park, M. J. Cha, Y. Yi, A. Song, K. B. Chung, J. H. Seo, and B. Walker, *RSC Adv.* **9**, 20670 (2019).
- ³⁷F. Huang, L. Hou, H. Wu, X. Wang, H. Shen, W. Cao, W. Yang, and Y. Cao, *J. Am. Chem. Soc.* **126**, 9845 (2004).
- ³⁸H. He, C. Zhang, X. Xu, L. Zhang, L. Huang, J. Chen, H. Wu, and Y. Cao, *Adv. Mater.* **23**, 3086 (2011).
- ³⁹Y. Zhou, C. Fuentes-Hernandez, J. Shim, J. Meyer, A. J. Giordano, H. Li, P. Winget, T. Papadopoulos, H. Cheun, J. Kim, M. Fenoll, A. Dindar, W. Haskes, E. Najafabadi, T. M. Khan, H. Sojoudi, S. Barlow, S. Graham, J. L. Brédas, S. R. Marder, A. Kahn, and B. Kippelen, *Science* **336**, 327 (2012).
- ⁴⁰J. H. Kang, A. K. Harit, J. E. Jeong, H. Y. Woo, J. H. Seo, and B. Walker, *Solar RRL* **5**, 2100521 (2021).
- ⁴¹A. Guerrero, S. Chambon, L. Hirsch, and G. Garcia-Belmonte, *Adv. Funct. Mater.* **24**, 6234 (2014).
- ⁴²A. K. K. Kyaw, X. W. Sun, C. Y. Jiang, G. Q. Lo, D. W. Zhao, and D. L. Kwong, *Appl. Phys. Lett.* **93**, 221107 (2008).
- ⁴³M. S. White, D. C. Olson, S. E. Shaheen, N. Kopidakis, and D. S. Ginley, *Appl. Phys. Lett.* **89**, 143517 (2006).
- ⁴⁴Irfan, H. Ding, Y. Gao, C. Small, D. Y. Kim, J. Subbiah, and F. So, *Appl. Phys. Lett.* **96**, 243307 (2010).
- ⁴⁵K. V. Chauhan, P. Sullivan, J. L. Yang, and T. S. Jones, *J. Phys. Chem. C* **114**, 3304 (2010).
- ⁴⁶J. R. Manders, S.-W. Tsang, M. J. Hartel, T.-H. Lai, S. Chen, C. M. Amb, J. R. Reynolds, and F. So, *Adv. Funct. Mater.* **23**, 2993 (2013).
- ⁴⁷M. D. Irwin, J. D. Servaites, D. B. Buchholz, B. J. Leever, J. Liu, J. D. Emery, M. Zhang, J. H. Song, M. F. Durstock, A. J. Freeman, M. J. Bedzyk, M. C. Hersam, R. P. H. Chang, M. A. Ratner, and T. J. Marks, *Chem. Mater.* **23**, 2218 (2011).
- ⁴⁸J. Bouclé, P. Ravirajan, and J. Nelson, *J. Mater. Chem.* **17**, 3141 (2007).
- ⁴⁹S. Chen, J. R. Manders, S. W. Tsang, and F. So, *J. Mater. Chem.* **22**, 24202 (2012).
- ⁵⁰H. C. Liao, C. S. Tsao, T. H. Lin, M. H. Jao, C. M. Chuang, S. Y. Chang, Y. C. Huang, Y. T. Shao, C. Y. Chen, C. J. Su, U. S. Jeng, Y. F. Chen, and W. F. Su, *ACS Nano* **6**, 1657 (2012).
- ⁵¹H. C. Chen, C. W. Lai, I. C. Wu, H. R. Pan, I. W. P. Chen, Y. K. Peng, C. L. Liu, C. H. Chen, and P. T. Chou, *Adv. Mater.* **23**, 5451 (2011).
- ⁵²A. G. Ricciardulli, S. Yang, X. Feng, and P. W. M. Blom, *ACS Appl. Mater. Interfaces* **9**, 25412 (2017).
- ⁵³Z. Liu, J. Li, Z. H. Sun, G. Tai, S. P. Lau, and F. Yan, *ACS Nano* **6**, 810 (2012).
- ⁵⁴Y. Wang, S. W. Tong, X. F. Xu, B. Özyilmaz, and K. P. Loh, *Adv. Mater.* **23**, 1514 (2011).

- ⁵⁵Y. Terao, H. Sasabe, and C. Adachi, *Appl. Phys. Lett.* **90**, 103515 (2007).
- ⁵⁶D. M. Guldin, *Phys. Chem. Chem. Phys.* **9**, 1400 (2007).
- ⁵⁷J. M. Lee, J. S. Park, S. H. Lee, H. Kim, S. Yoo, and S. O. Kim, *Adv. Mater.* **23**, 629 (2011).
- ⁵⁸J. H. Kang, S. Choi, Y. J. Park, J. S. Park, N. S. Cho, S. Cho, B. Walker, D. S. Choi, J. W. Shin, and J. H. Seo, *Carbon* **171**, 341 (2021).
- ⁵⁹S. Albrecht, S. Yilmaz, I. Dumsch, S. Allard, U. Scherf, S. Beaupré, M. Leclerc, and D. Neher, *Energy Procedia* **31**, 159 (2012).
- ⁶⁰T. Aernouts, T. Aleksandrov, C. Girotto, J. Genoe, and J. Poortmans, *Appl. Phys. Lett.* **92**, 033306 (2008).
- ⁶¹C. N. Hoth, P. Schilinsky, S. A. Choulis, and C. J. Brabec, *Nano Lett.* **8**, 2806 (2008).
- ⁶²S. Günes, H. Neugebauer, and N. S. Sariciftci, *Chem. Rev.* **107**, 1324 (2007).
- ⁶³Y. Galagan, E. W. C. Coenen, R. Abbel, T. J. Van Lammeren, S. Sabik, M. Barink, E. R. Meinders, R. Andriessen, and P. W. M. Blom, *Org. Electron.* **14**, 38 (2013).
- ⁶⁴S. Y. Leblebici, T. L. Chen, P. Olalde-Velasco, W. Yang, and B. Ma, *ACS Appl. Mater. Interfaces* **5**, 10105 (2013).
- ⁶⁵T. F. Hinrichsen, C. C. S. Chan, C. Ma, D. Paleček, A. Gillett, S. Chen, X. Zou, G. Zhang, H. L. Yip, K. S. Wong, R. H. Friend, H. Yan, A. Rao, and P. C. Y. Chow, *Nat. Commun.* **11**, 5617 (2020).
- ⁶⁶R. Stein, F. R. Kogler, and C. J. Brabec, *J. Mater. Chem.* **20**, 2499 (2010).
- ⁶⁷J. J. Intemann, K. Yao, Y. X. Li, H. L. Yip, Y. X. Xu, P. W. Liang, C. C. Chueh, F. Z. Ding, X. Yang, X. Li, Y. Chen, and A. K. Y. Jen, *Adv. Funct. Mater.* **24**, 1465 (2014).
- ⁶⁸C. Yi, X. Hu, X. Gong, and A. Elzatahry, *Mater. Today* **19**, 169 (2016).
- ⁶⁹S. Narioka, H. Ishii, D. Yoshimura, M. Sei, Y. Ouchi, K. Seki, S. Hasegawa, T. Miyazaki, Y. Harima, and K. Yamashita, *Appl. Phys. Lett.* **67**, 1899 (1995).
- ⁷⁰H. Ishii, K. Sugiyama, E. Ito, and K. Seki, *Adv. Mater.* **11**, 605 (1999).
- ⁷¹N. Kosuci and H. Kuroda, *Chem. Phys.* **39**, 337 (1979).
- ⁷²P. A. Bennett and J. C. Fugle, *Phys. Rev. B* **26**, 6030 (1982).
- ⁷³F. De Groot, *Chem. Rev.* **101**, 1779 (2001).
- ⁷⁴J. Singh, C. Lamberti, and J. A. Van Bokhoven, *Chem. Soc. Rev.* **39**, 4754 (2010).
- ⁷⁵J. Liu, S. Chen, D. Qian, B. Gautam, G. Yang, J. Zhao, J. Bergqvist, F. Zhang, W. Ma, H. Ade, O. Inganäs, K. Gundogdu, F. Gao, and H. Yan, *Nat. Energy* **1**, 16089 (2016).
- ⁷⁶C. Yang, S. Zhang, J. Ren, M. Gao, P. Bi, L. Ye, J. Hou, S. Zhang, L. Ye, and J. Hou, *Energy Environ. Sci.* **13**, 2864 (2020).
- ⁷⁷Z. Zheng, Q. Hu, S. Zhang, D. Zhang, J. Wang, S. Xie, R. Wang, Y. Qin, W. Li, L. Hong, N. Liang, F. Liu, Y. Zhang, Z. Wei, Z. Tang, T. P. Russell, J. Hou, and H. Zhou, *Adv. Mater.* **30**, 1801801 (2018).
- ⁷⁸C. Zhu, J. Yuan, F. Cai, L. Meng, H. Zhang, H. Chen, J. Li, B. Qiu, H. Peng, S. Chen, Y. Hu, C. Yang, F. Gao, Y. Zou, and Y. Li, *Energy Environ. Sci.* **13**, 2459 (2020).
- ⁷⁹B. Xiao, A. Tang, J. Zhang, A. Mahmood, Z. Wei, and E. Zhou, *Adv. Energy Mater.* **7**, 1602269 (2017).
- ⁸⁰H. Fu, Z. Wang, and Y. Sun, *Angew. Chem.* **131**, 4488 (2019).
- ⁸¹Y. Zheng, J. Huang, G. Wang, J. Kong, D. Huang, M. Mohadjer Beromi, N. Hazari, A. D. Taylor, and J. Yu, *Mater. Today* **21**, 79 (2018).
- ⁸²J. Yuan, Y. Zhang, L. Zhou, G. Zhang, H. L. Yip, T. K. Lau, X. Lu, C. Zhu, H. Peng, P. A. Johnson, M. Leclerc, Y. Cao, J. Ulanski, Y. Li, and Y. Zou, *Joule* **3**, 1140 (2019).
- ⁸³Y. Lin, A. Magomedov, Y. Firdaus, D. Kaltsas, A. El-Labban, H. Faber, D. R. Naphade, E. Yengel, X. Zheng, E. Yarali, N. Chaturvedi, K. Loganathan, D. Gkeka, S. H. AlShammari, O. M. Bakr, F. Laquai, L. Tsetseris, V. Getautis, and T. D. Anthopoulos, *ChemSusChem* **14**, 3569 (2021).
- ⁸⁴G. H. Jun, S. H. Jin, B. Lee, B. H. Kim, W. S. Chae, S. H. Hong, and S. Jeon, *Energy Environ. Sci.* **6**, 3000 (2013).
- ⁸⁵Y. Han, H. Dong, W. Pan, B. Liu, X. Chen, R. Huang, Z. Li, F. Li, Q. Luo, J. Zhang, Z. Wei, and C. Q. Ma, *ACS Appl. Mater. Interfaces* **13**, 17869 (2021).
- ⁸⁶Q. Wang, Y. Zhou, H. Zheng, J. Shi, C. Li, C. Q. Su, L. Wang, C. Luo, D. Hu, J. Pei, J. Wang, J. Peng, and Y. Cao, *Org. Electron.* **12**, 1858 (2011).
- ⁸⁷I. G. Hill, A. Rajagopal, A. Kahn, and Y. Hu, *Appl. Phys. Lett.* **73**, 662 (1998).
- ⁸⁸A. J. Mäkinen, I. G. Hill, M. Kinoshita, T. Noda, Y. Shirota, and Z. H. Kafafi, *J. Appl. Phys.* **91**, 5456 (2002).
- ⁸⁹H. Ishii and K. Seki, *Synth. Met.* **91**, 137 (1997).
- ⁹⁰S. Olthof, *APL Mater.* **4**, 091502 (2016).
- ⁹¹M. Borgwardt, S. T. Omelchenko, M. Favaro, P. Plate, C. Höhn, D. Abou-Ras, K. Schwarzburg, R. van de Krol, H. A. Atwater, N. S. Lewis, R. Eichberger, and D. Friedrich, *Nat. Commun.* **10**, 2106 (2019).
- ⁹²M. Muench, E. Mankel, T. Mayer, and W. Jaegermann, *Adv. Mater. Technol.* **6**, 2000110 (2021).
- ⁹³W. Lee, J. H. Seo, and H. Y. Woo, *Polymer* **54**, 5104 (2013).
- ⁹⁴H. J. Bolink, H. Brine, E. Coronado, and M. Sessolo, *ACS Appl. Mater. Interfaces* **2**, 2694 (2010).
- ⁹⁵J. H. Seo, E. B. Namdas, A. Gutacker, A. J. Heeger, and G. C. Bazan, *Appl. Phys. Lett.* **97**, 043303 (2010).
- ⁹⁶Y. Wang, B. Liu, A. Mikhailovsky, and G. C. Bazan, *Adv. Mater.* **22**, 656 (2010).
- ⁹⁷J. H. Seo, A. Gutacker, B. Walker, S. Cho, A. Garcia, R. Yang, T. Q. Nguyen, A. J. Heeger, and G. C. Bazan, *J. Am. Chem. Soc.* **131**, 18220 (2009).
- ⁹⁸K. G. Lim, S. M. Park, H. Y. Woo, and T. W. Lee, *ChemSusChem* **8**, 3062 (2015).
- ⁹⁹Q. Cui and G. C. Bazan, *Acc. Chem. Res.* **51**, 202 (2018).
- ¹⁰⁰G. Feng, C. K. Mai, R. Zhan, G. C. Bazan, and B. Liu, *J. Mater. Chem. B* **3**, 7340 (2015).
- ¹⁰¹H. Liu, L. Huang, X. Cheng, A. Hu, H. Xu, L. Chen, and Y. Chen, *ACS Appl. Mater. Interfaces* **9**, 1145 (2017).
- ¹⁰²H. Kang, S. Hong, J. Lee, and K. Lee, *Adv. Mater.* **24**, 3005 (2012).
- ¹⁰³S. Lee, S. Park, N. Sylvianti, H. K. Choi, and J. H. Kim, *Synth. Met.* **209**, 441 (2015).
- ¹⁰⁴C. C. Chang, J. H. Tao, C. E. Tsai, Y. J. Cheng, and C. S. Hsu, *ACS Appl. Mater. Interfaces* **10**, 21466 (2018).
- ¹⁰⁵J. Cameron and P. J. Skabar, *Mater. Horiz.* **7**, 1759 (2020).
- ¹⁰⁶V. Lami, Y. J. Hofstetter, J. F. Butscher, and Y. Vaynzof, *Adv. Electron. Mater.* **6**, 2000213 (2020).
- ¹⁰⁷W. Teng, C. H. Li, W. C. Lo, Y. S. Tsai, C. Y. Liao, Y. W. You, H. L. Ho, W. L. Li, C. C. Lee, W. C. Lin, and Y. M. Chang, *Solar RRL* **4**, 2000223 (2020).
- ¹⁰⁸J. K. Chang, D. L. Lin, J. Bin Yang, Y. W. Yang, W. S. Tseng, and M. H. Chen, *Phys. Status Solidi A* **218**, 2000584 (2021).
- ¹⁰⁹Y. Yin, X. Pan, M. R. Andersson, D. A. Lewis, and G. G. Andersson, *Adv. Mater. Interfaces* **8**, 2101657 (2021).
- ¹¹⁰B. Walker, H. Choi, and J. Y. Kim, *Curr. Appl. Phys.* **17**, 370 (2017).
- ¹¹¹N. Tokmoldin, N. Griffiths, D. D. C. Bradley, and S. A. Hague, *Adv. Mater.* **21**, 3475 (2009).
- ¹¹²K. Zilberman, S. Trost, J. Meyer, A. Kahn, A. Behrendt, D. Lützenkirchen-Hecht, R. Frahm, and T. Riedl, *Adv. Funct. Mater.* **21**, 4776 (2011).
- ¹¹³J. Li, S. Kim, S. Edlington, J. Neddy, S. Cho, K. Lee, A. J. Heeger, M. C. Gupta, and J. T. Yates, *Sol. Energy Mater. Sol. Cells* **95**, 1123 (2011).
- ¹¹⁴K. X. Steirer, J. P. Chasin, N. E. Widjonarko, J. J. Berry, A. Miedaner, D. S. Ginley, and D. C. Olson, *Org. Electron.* **11**, 1414 (2010).
- ¹¹⁵Z. Tan, D. Qian, W. Zhang, L. Li, Y. Ding, Q. Xu, F. Wang, and Y. Li, *J. Mater. Chem. A* **1**, 657 (2013).
- ¹¹⁶K. Zilberman, H. Gharbi, A. Behrendt, S. Trost, and T. Riedl, *ACS Appl. Mater. Interfaces* **4**, 1164 (2012).
- ¹¹⁷H. N. Tran, S. Park, F. T. A. Wibowo, N. V. Krishna, J. H. Kang, J. H. Seo, H. Nguyen-Phu, S. Y. Jang, and S. Cho, *Adv. Sci.* **7**, 2002395 (2020).
- ¹¹⁸L. K. Jagadamma, M. Abdelsamie, A. El Labban, E. Aresu, G. O. Ngongang Ndjawa, D. H. Anjum, D. Cha, P. M. Beaujuge, and A. Amassian, *J. Mater. Chem. A* **2**, 13321 (2014).
- ¹¹⁹Y. Sun, J. H. Seo, C. J. Takacs, J. Seifter, and A. J. Heeger, *Adv. Mater.* **23**, 1679 (2011).
- ¹²⁰S. K. Hau, H. L. Yip, N. S. Baek, J. Zou, K. O'Malley, and A. K. Y. Jen, *Appl. Phys. Lett.* **92**, 253301 (2008).
- ¹²¹M. B. Upama, N. K. Elumalai, M. A. Mahmud, C. Xu, D. Wang, M. Wright, and A. Uddin, *Sol. Energy Mater. Sol. Cells* **187**, 273 (2018).

- ¹²²Y. Jung, W. Yang, C. Y. Koo, K. Song, and J. Moon, *J. Mater. Chem.* **22**, 5390 (2012).
- ¹²³S. Ullah Awan, S. K. Hasanaain, M. F. Bertino, and G. Hassnain Jaffari, *J. Appl. Phys.* **112**, 103924 (2012).
- ¹²⁴H. Li, L. K. Schirra, J. Shim, H. Cheun, B. Kippelen, O. L. A. Monti, and J. L. Bredas, *Chem. Mater.* **24**, 3044 (2012).
- ¹²⁵S. H. Park, A. Roy, S. Beaupré, S. Cho, N. Coates, J. S. Moon, D. Moses, M. Leclerc, K. Lee, and A. J. Heeger, *Nat. Photonics* **3**, 297 (2009).
- ¹²⁶C. Waldau, M. Morana, P. Denk, P. Schilinsky, K. Coakley, S. A. Choulis, and C. J. Brabec, *Appl. Phys. Lett.* **89**, 233517 (2006).
- ¹²⁷M. Mirsafaei, P. B. Jensen, M. Ahmadpour, H. Lakhotiya, J. L. Hansen, B. Julsgaard, H. G. Rubahn, R. Lazzari, N. Witkowski, P. Balling, and M. Madsen, *ACS Appl. Energy Mater.* **3**, 253 (2020).
- ¹²⁸D. Amelot, M. Ahmadpour, Q. Ros, H. Cruguel, N. Casaretto, A. Cossaro, L. Floreano, M. Madsen, and N. Witkowski, *ACS Appl. Mater. Interfaces* **13**, 19460 (2021).
- ¹²⁹M. Thambidurai, F. Shini, J. Y. Kim, C. Lee, and C. Dang, *Mater. Lett.* **274**, 128003 (2020).
- ¹³⁰B. A. Odeke, G. D. Chung, J. A. Fajemisin, K. S. Suraj, D. K. Tonui, A. R. Tobi, T. C. Bewale, J. A. Ajibola, and N. Y. Dzade, *Materials* **13**, 5765 (2020).
- ¹³¹V. D. Patel, R. Dhar, N. Gandhi, S. R. Meher, and D. Gupta, *J. Electron. Mater.* **51**, 601 (2022).
- ¹³²E. J. Lee, S. W. Heo, Y. W. Han, and D. K. Moon, *J. Mater. Chem. C* **4**, 2463 (2016).
- ¹³³J. Subbiah, V. D. Mitchell, N. K. C. Hui, D. J. Jones, and W. W. H. Wong, *Angew. Chemie - Int. Ed.* **56**, 8431 (2017).
- ¹³⁴X. Liu, Y. Wu, X. Li, W. Zhang, L. Zhao, H. Q. Wang, and J. Fang, *J. Mater. Chem. A* **4**, 297 (2016).
- ¹³⁵X. Mu, X. Yu, D. Xu, X. Shen, Z. Xia, H. He, H. Zhu, J. Xie, B. Sun, and D. Yang, *Nano Energy* **16**, 54 (2015).
- ¹³⁶L. Lin, K. M. Boopathi, J. Ding, C. W. Chu, and C. C. Chang, *FlatChem* **5**, 18 (2017).
- ¹³⁷A. Kyndiah, A. Ablat, S. Guyot-Reeb, T. Schultz, F. Zu, N. Koch, P. Amsalem, S. Chioldini, T. Yilmaz Alic, Y. Topal, M. Kus, L. Hirsch, S. Fasquel, and M. Abbas, *Sci. Rep.* **8**, 10946 (2018).
- ¹³⁸Y. M. Chang and C. Y. Leu, *J. Mater. Chem. A* **1**, 6446 (2013).
- ¹³⁹R. Schlesinger, F. Bianchi, S. Blumstengel, C. Christodoulou, R. Ovsyannikov, B. Kobin, K. Moudgil, S. Barlow, S. Hecht, S. R. Marder, F. Henneberger, and N. Koch, *Nat. Commun.* **6**, 6754 (2015).
- ¹⁴⁰S. Pang, Y. Hernandez, X. Feng, and K. Müllen, *Adv. Mater.* **23**, 2779 (2011).
- ¹⁴¹S. Bae, H. Kim, Y. Lee, X. Xu, J. S. Park, Y. Zheng, J. Balakrishnan, T. Lei, H. Ri Kim, Y. Il. Song, Y. J. Kim, K. S. Kim, B. Özylmaz, J. H. Ahn, B. H. Hong, and S. Iijima, *Nat. Nanotechnol.* **5**, 574 (2010).
- ¹⁴²K. S. Kim, Y. Zhao, H. Jang, S. Y. Lee, J. M. Kim, K. S. Kim, J. H. Ahn, P. Kim, J. Y. Choi, and B. H. Hong, *Nature* **457**, 706 (2009).
- ¹⁴³W. Ke, G. Fang, Q. Liu, L. Xiong, P. Qin, H. Tao, J. Wang, H. Lei, B. Li, J. Wan, G. Yang, and Y. Yan, *J. Am. Chem. Soc.* **137**, 6730 (2015).
- ¹⁴⁴V. H. Tran, R. Khan, I. H. Lee, and S. H. Lee, *Sol. Energy Mater. Sol. Cells* **179**, 260 (2018).
- ¹⁴⁵M. Watanabe, M. L. Thomas, S. Zhang, K. Ueno, T. Yasuda, and K. Dokko, *Chem. Rev.* **117**, 7190 (2017).
- ¹⁴⁶D. R. Macfarlane, N. Tachikawa, M. Forsyth, J. M. Pringle, P. C. Howlett, G. D. Elliott, J. H. Davis, M. Watanabe, P. Simon, and C. A. Angell, *Energy Environ. Sci.* **7**, 232 (2014).
- ¹⁴⁷B. R. Lee, H. Choi, J. Sunpark, H. J. Lee, S. O. Kim, J. Y. Kim, and M. H. Song, *J. Mater. Chem.* **21**, 2051 (2011).
- ¹⁴⁸W. Yu, L. Huang, D. Yang, P. Fu, L. Zhou, J. Zhang, and C. Li, *J. Mater. Chem. A* **3**, 10660 (2015).
- ¹⁴⁹Y. Yang, Q. Kang, Q. Liao, Z. Zheng, C. He, B. Xu, and J. Hou, *ACS Appl. Mater. Interfaces* **12**, 39462 (2020).